Title Page

IRGM/Irgm1 Aggravates Progression of Atherosclerosis by Inducing Macrophage Apoptosis

Running Title: IRGM/Irgm1 Aggravates Atherosclerosis

Shaohong Fang[1,2†], Song Sun[2,3†], Hengxuan Cai[1,2†], Xinran Hao[2,3], Xiaoyi Zou[2,3], Xin Wan[2,3], Jiangtian Tian[1,2], Zhaoying Li[1,2], Shanjie Wang[1,2], Zhongze He[2,3], Wei Huang[2,3], Chenchen Liang[1,2], Zhenming Zhang[1,2], Liming Yang[4], Jinwei Tian[1,2*], Bo Yu[1,2*] and Bo Sun[2,3*]

[1]Department of Cardiology, Second Affiliated Hospital of Harbin Medical University, Harbin 150086, China;

[2]The Key Laboratory of Myocardial Ischemia, Chinese Ministry of Education, Harbin 150086, China;

[3]Department of Neurobiology, Harbin Medical University; Neurobiology Key Laboratory, Education Department of Heilongjiang Province, Harbin 150086, China;

[4]Department of Pathophysiology, Harbin Medical University-Daqing, Daqing 163319, China

[†]The first 3 authors contributed equally to this article.

[*]**Address for correspondence:**

Bo Sun, 158 Baojian Road, Nangang District, 150086 Harbin, China. Tel: +86 451 8827 2363, Fax: +86 451 8827 2363, Email: sunbohmu@163.com;

Bo Yu, 246 Xuefu Road, Nangang District, 150086 Harbin, China. Tel: +86 451 8660 5180, Fax: +86 451 8660 5180, Email: dryu_hmu@163.com;

Jinwei Tian, 246 Xuefu Road, Nangang District, 150086 Harbin, China. Tel: +86 451 8660 5800, Fax: +86 451 8660 5800, Email: tianjinweidr2009@163.com.

Word count: 11,895

The authors have declared that no conflict of interest exists.

Abstract

Acute coronary syndrome (ACS) caused by plaque rupture (PR) is the chief culprit behind cardiovascular death, yet its exact mechanism remains unclear. Immunity-related GTPase (IRGM/Irgm1) has been widely studied in several inflammatory diseases, but the role of IRGM/Irgm1 in atherosclerosis is poorly characterized. Here, we shed light on the mechanism by which IRGM/Irgm1 contributes to plaque vulnerability in atherosclerosis. We first identified ruptured and non-ruptured plaques by optical coherence tomography, and strikingly found that serum IRGM was highly expressed in ST-segment elevation myocardial infarction patients with PR. Next, we used ApoE$^{-/-}$Irgm1$^{+/+}$ and ApoE$^{-/-}$Irgm1$^{+/-}$ mice and corresponding bone marrow chimeras to establish a model for advanced atherosclerosis, and found that Irgm1 could aggravate progression of atherosclerotic plaques. We confirmed that Irgm1 contributes to macrophage apoptosis by promoting the production of reactive oxygen species. Finally, we discovered that Irgm1 induces macrophage apoptosis by activating the MAPK signaling pathway. Our findings highlight the mechanism by which IRGM/Irgm1 contributes to the formation of vulnerable plaques and may offer a novel target for the timely treatment of ACS.

Introduction

Atherosclerosis is a chronic inflammatory disease that occurs in the arterial wall. Its related complication, acute coronary syndrome (ACS), is currently the most common cause of morbidity and mortality worldwide (1). There are three main pathological mechanisms leading to ACS, namely plaque rupture (PR), plaque erosion (PE), and calcified nodules (CN) (2, 3). Traditionally, research on these pathological mechanisms of ACS has mostly relied on autopsy (4). In the current era, the development of intracoronary optical coherence tomography (OCT), a diagnostic modality with high spatial resolution, makes it possible to accurately identify the plaque morphologies of patients *in vivo* as well as to deeply explore the underlying pathogenesis of atherosclerotic plaque progression (5). Previously, our research group used OCT to assess the distribution of culprit plaque in ACS patients *in vivo* and confirmed that PR has the highest incidence among the three pathological mechanisms above (6). We further identified *in vivo* that plaques that tend to rupture are mostly vulnerable plaques with thin fibrous caps and large lipid burdens (7). We deduce that increased plaque vulnerability is closely related to PR and the subsequent occurrence of ACS, which is life-threatening. Therefore, it is of vital importance to study the factors that influence pathogenesis of atherosclerotic vulnerable plaques, and the underlying mechanisms. A large number of clinical trials conducted by our group, in parallel with those of other groups, have suggested that age, smoking, hypertension, chronic kidney disease, and dyslipidemia are associated with plaque vulnerability (8-11). However, the exact

mechanism that influences the vulnerability of atherosclerotic plaques remains unclear at a molecular level.

The Immunity-related GTPase, named IRGM in humans and Irgm1 in mice, belongs to a family of IFN-γ-inducible GTPases (12, 13). A role for IRGM/Irgm1 in inflammatory bowel disease, tumors, and other diseases has been widely reported, yet few studies have focused on IRGM/Irgm1 in the field of atherosclerotic disease (14, 15). Previously, we found that Irgm1 can influence the progression of atherosclerotic plaques by regulating the uptake of oxidized low-density lipoprotein (ox-LDL) by macrophages and the formation of foam cells (16). We have also shown that IRGM/Irgm1 can promote the polarization of M1 subtype macrophages and thus aggravate the progression of atherosclerotic plaque, which was then confirmed in both clinical patients and Irgm1 knockdown mice (17). Accordingly, IRGM/Irgm1 expressed in macrophages can promote the progression of atherosclerotic plaques. Nevertheless, the precise mechanism by which IRGM/Irgm1 regulates plaque vulnerability by acting through macrophages remains unclear.

The progression of atherosclerotic plaque is known to involve infiltration by macrophages, formation of a lipid necrotic core, and deposition of cholesterol crystals (18, 19). As the primary immune cells within atherosclerotic plaques, macrophages play a vital role in regulating their development and stability during plaque progression (20, 21). Previous studies have shown that there are excessive numbers of apoptotic macrophages in vulnerable plaques (22). Abundant evidence also confirms that

macrophage apoptosis directly causes plaque instability and increases the risk of adverse cardiovascular events (23-25). Therefore, a search for the underlying upstream target that regulates macrophage apoptosis has important clinical implications for assessing the risk of vulnerable plaque formation in patients with atherosclerosis.

In the present study, we used OCT to assess the morphological features of culprit plaques in patients with ST-segment elevation myocardial infarction (STEMI), and classified the patients according to the existence of PR *in vivo*. Serum studies revealed that IRGM was highly expressed in patients with ruptured plaques (the RUP group). Meanwhile, expression of IRGM was correlated with PR in STEMI patients, which can thus be regarded as a potential factor contributing to PR. Subsequently, we further clarified *in vivo* that Irgm1 was able to modify the phenotype and exacerbate the progression of atherosclerotic plaques. Finally, we verified that the mechanism by which Irgm1 contributes to the progression of atherosclerosis is by promoting apoptosis in macrophages. This study will provide a new pleiotropic role for IRGM/Irgm1 in the progression of atherosclerotic plaque and unveil novel potential targets for the prevention and treatment of atherosclerosis.

Results

Serum IRGM is correlated with atherosclerotic PR events in STEMI patients. Initially, we investigated whether serum Irgm1 is associated with atherosclerotic PR in STEMI patients. The study flow chart is shown in Figure 1. Among 85 STEMI patients with analyzable OCT images, PR was identified as the underlying pathology in 52 subjects (61.2%). Figure 2A shows representative OCT images of normal vessels and culprit sites of plaques in the RUP and NO-RUP groups. Supplemental Table 1 lists a comparison of baseline clinical characteristics between the RUP and NO-RUP groups. It was shown that serum LDL-C and total cholesterol (TC) levels were higher in the patients with PR, while no significant differences were observed in other indicators. Plaque characteristics as assessed by OCT are presented in Supplemental Table 2. It was demonstrated that the prevalence of thin-cap fibroatheroma (TCFA) and lipid-rich plaque was higher, and the minimum fibrous cap was thinner in the RUP group.

Subsequently, the level of serum IRGM was quantified by ELISA. It was found that serum IRGM levels differed significantly among the three groups. The serum IRGM level of patients in the RUP group was the highest, while that of healthy volunteers was the lowest (Figure 2B).

We next evaluated the ability of serum IRGM level as a predictor of PR in patients with STEMI (Figure 2C). Without adjusting for any factors, IRGM was a strong risk factor, with an odds ratio (OR) of 1.23 (95% confidence interval (CI): 1.06~1.43, p=0.006).

As baseline characteristics differed between these two groups, we adjusted factors in 4 different models: model 1, a logistic regression model adjusted for age; model 2, in which model 1 was further adjusted for hypertension, diabetes mellitus, and current smoking; model 3, in which model 2 was additionally adjusted for lipid factors (LDL-C and TC); and model 4, in which model 3 was further adjusted for peak troponin I (TnI) and high-sensitivity C-reactive protein (hs-CRP). After each increase in the adjustment factors of the models, IRGM remains an effective predictor of PR, with an OR of 1.28 (95% CI: 1.06~1.54, p=0.012) in model 4. Thus, serum IRGM potentially predicts atherosclerotic PR events in subjects with STEMI, independent of LDL-C and TC levels.

IRGM is highly expressed in patients with atherosclerotic plaque. To detect the expression of IRGM in atherosclerotic plaques, we analyzed the plaque morphology of median arteries from patients with and without atherosclerosis. Immunohistochemistry was used to observe the expression of IRGM and CD68 in intravascular intimal plaques. The results showed that the expression of IRGM and CD68 in atherosclerotic plaques and their proportion in plaques were significantly increased (Figure 2D–2F). At the same time, we found that regions with high levels of IRGM also tended to display expression of CD68. Therefore, we analyzed the correlation between the expression of IRGM and CD68 in the plaques (Supplemental Figure 2F) and found that the expression of CD68 and IRGM was positively correlated. Together, these results indicated that

IRGM was highly expressed in atherosclerotic plaques and mostly exists in $CD68^{+}$ macrophages within the plaques.

Irgm1 can affect atherosclerotic lesion phenotype in vivo. To investigate whether Irgm1 plays a role in the pathogenesis of atherosclerosis *in vivo*, we first distinguished $ApoE^{-/-}Irgm1^{+/-}$ and $ApoE^{-/-}Irgm1^{+/+}$ mice by genotypic analysis (Figure 3A). Furthermore, the knockdown efficiency of Irgm1 at the gene level was determined in 11 major organs or cell types of mice by qPCR analysis. The results showed that, compared with $ApoE^{-/-}Irgm1^{+/+}$ genotype, $ApoE^{-/-}Irgm1^{+/-}$ mice had significantly reduced Irgm1 expression in these organs or cells (Supplemental Figure 3A). After a Western diet for 16 weeks (Figure 3B), mice presented with atherosclerotic lesions positive for oil-red O (ORO) staining in the aorta. There was no difference in the extent of the positive staining area of the aortic arch, while the areas in both the thoracic and abdominal parts were significantly reduced in the $ApoE^{-/-}Irgm1^{+/-}$ group (Supplemental Figure 3B). Meanwhile, we analyzed the percentage of ORO positive areas in the aortic lumen area in the aortic arch, thoracic aorta, and abdominal aorta. The results showed that the percentage of the aortic ORO positive areas in $ApoE^{-/-}Irgm1^{+/-}$ mice were significantly reduced (Figure 3C–D). Subsequently, H&E staining was used to analyze differences between these two groups in the thickness of the fibrous cap, the area of the plaque, and the size of the necrotic core within the aortic sinus (Figure 3E). Our results showed that compared with mice in the $ApoE^{-/-}Irgm1^{+/+}$ group, mice in the $ApoE^{-/-}$ $Irgm1^{+/-}$ group

had a thicker fibrous cap, reduced necrotic core area and necrotic core ratio, although there was no significant difference in lesion areas between the two groups (Figure 3F–G, 3J; Supplemental Figure 3C). Next, we observed the content of neutral lipids in the aortic sinus of mice by ORO staining. We found that the content and percentage of neutral lipids in ApoE$^{-/-}$Irgm1$^{+/-}$ mice were significantly lower than those in ApoE$^{-/-}$Irgm1$^{+/+}$ mice (Figure 3H, 3K; Supplemental Figure 3E). Masson staining was used to measure the collagen fiber content in the aortic sinus plaque of mice. The results showed that compared with ApoE$^{-/-}$Irgm1$^{+/+}$ mice, the proportion of collagen content in ApoE$^{-/-}$Irgm1$^{+/-}$ mice was significantly increased (Figure 3I, 3L, Supplemental Figure 3F). Cholesterol crystals in the aortic sinus plaque were further examined by laser reflection microscopy, and ApoE$^{-/-}$Irgm1$^{+/+}$ mice showed significantly fewer cholesterol crystals (Figure 3M–N). These results suggest that Irgm1 can aggravate the progression of atherosclerotic plaques *in vivo*.

Irgm1 induces apoptosis in macrophages. Several previous studies have demonstrated that there is a large amount of macrophage infiltration during the development of atherosclerosis (26, 27). We first observed the relationship between Irgm1 and macrophage autophagy *in vitro* (Supplemental Figure 1). After stimulating the RAW264.7 macrophage cell line with oxidized LDL (ox-LDL) for 3 h, we found that the fluorescence signals of autophagosomes and lysosomes could be combined successfully (Supplemental Figure 1D–E). However, after stimulating the RAW264.7

cell line with ox-LDL for 48 h, we were disappointed to find that the autophagic flux was blocked (Supplemental Figure 1F–G). Excessive apoptosis of macrophages is a noticeable feature of vulnerable plaques (22). We next asked whether Irgm1 is involved in macrophage apoptosis during the progression of atherosclerosis. Initially, TUNEL staining was used to label apoptosis within aortic sinus plaques in ApoE$^{-/-}$Irgm1$^{+/+}$ and ApoE$^{-/-}$Irgm1$^{+/-}$ mice. The results suggested that the proportion of TUNEL-positive cells in ApoE$^{-/-}$Irgm1$^{+/+}$ mice was significantly higher than that in ApoE$^{-/-}$Irgm1$^{+/-}$ mice (Figure 4A–B). We further observed by immunohistochemistry that the expression of cleaved-caspase3 and cleaved-caspase9 in the plaque of ApoE$^{-/-}$Irgm1$^{+/-}$ mice was significantly lower than that of ApoE$^{-/-}$ Irgm1$^{+/+}$ mice (Figure 4C–E). We conclude that Irgm1 can induce apoptosis in plaques. We then assessed whether Irgm1 could induce macrophage apoptosis *in vitro*. We silenced Irgm1 (si-Irgm1) by transfection to downregulate its expression. qPCR was used to verify the silencing efficiency. The results showed that the silencing efficiency of the si-Irgm1 group was significantly higher than that of the empty vehicle control (si-control) group (Supplemental Figure 1A). On this basis, we analyzed the activities of cleaved-caspase3/9 in the two groups mentioned above. The results showed that compared with the si-control group, the si-Irgm1 group showed lower activities of cleaved-caspase3 and cleaved-caspase9 (Figure 4F–G), which was in accordance with the findings at the protein level by western blot (Figure 4H–I). Furthermore, we used flow cytometry to detect apoptosis in mouse peritoneal macrophages. Compared with the apoptosis rate of peritoneal macrophages

in ApoE$^{-/-}$Irgm1$^{+/+}$ mice, those in ApoE$^{-/-}$Irgm1$^{+/-}$ mice showed a significantly reduced rate of apoptosis (Figure 4G, 4M). Finally, we co-localized cleaved-caspase3 and cleaved-caspase9 with CD11b in the plaques by immunofluorescence. The results showed that compared with ApoE$^{-/-}$Irgm1$^{+/+}$ mice, the co-localization ratio in the ApoE$^{-/-}$Irgm1$^{+/-}$ mice plaques was significantly reduced (Figure 4K–L, Figure 4N–O). In summary, we confirmed that Irgm1 can promote macrophage apoptosis both *in vivo* and *in vitro*.

ROS contributes to Irgm1-induced apoptosis in macrophages. Production and accumulation of ROS in macrophages can contribute to apoptosis (28). Thus, we used DHE fluorescent probes to label ROS production in the Raw264.7 macrophage cell line. Compared with the si-control group, the DHE fluorescence intensity of the si-Irgm1 group declined sharply (Figure 5A-5B). Subsequently, flow cytometry was used to detect the expression of intracellular ROS. The results showed that compared with the si-control group, the intracellular ROS intensity of the si-Irgm1 group was significantly reduced (Figure 5C-5D). Hence, Irgm1 can promote the production of intracellular ROS in macrophages. To further explore the role of ROS production promoted by Irgm1 in inducing macrophage apoptosis, we used western blotting to detect differences in the expression of apoptosis-related proteins and found that compared with the si-control group, the expression of cleaved-caspase3 and cleaved-caspase9 in the si-Irgm1 group was reduced. After adding the active oxygen scavenger N-acetyl cysteine (NAC) to the

si-Irgm1 group, cleaved-caspase3 and cleaved-caspase9 expression was further decreased (Figure 5E–5F). This is in line with the findings of cleaved-caspase3 and cleaved-caspase9 activities among these 3 groups of mice as detected by ultraviolet spectrophotometry (Figure 5G–5H). TUNEL staining was used to observe macrophage apoptosis. The results demonstrated that compared with the si-control group, the co-localized fluorescence intensity of TUNEL and DAPI in the si-Irgm1 group was significantly reduced. After adding the active oxygen scavenger NAC to the si-Irgm1 group, the co-localization fluorescence signal intensity of TUNEL and DAPI was further decreased (Figure 5I–5J). In summary, Irgm1 can lead to apoptosis in macrophages by promoting the production of ROS.

Irgm1 induces apoptosis in macrophages by activating MAPK signaling pathway. MAPK signaling has been implicated in apoptosis through the JNK/P38/ERK pathway in response to a variety of stress stimuli such as ROS (29). To explore the exact mechanism by which Irgm1 leads to macrophage apoptosis, western blotting was used to detect the essential proteins phosphorylated (p)-JNK, p-p38, and p-ERK in the MAPK signaling pathways, as well as the downstream apoptosis-related proteins Bax, Bcl2, cleaved-caspase3, and cleaved-caspase9. The results showed that compared with the si-control group, the expression of p-JNK, p-p38, p-ERK, Bax, cleaved-caspase3, and cleaved-caspase9 were significantly decreased in the si-Irgm1 group. In contrast, Bcl2 expression was increased (Figure 6A Lane 1,2 vs. Lane 3,4; Figure 6B–6C). After

adding NAC to the si-Irgm1 group, the expression of p-JNK, p-p38, p-ERK, and downstream apoptotic proteins Bax, cleaved-caspase3, and cleaved-caspase9 continued to decrease, and the expression of Bcl2 was further increased (Figure 6A Lane 5,6; Figure 6B–6C). Next, we investigated whether Irgm1 led to macrophage apoptosis through activation of the JNK/P38/ERK pathways in MAPK signaling. We first verified the efficiency of the three inhibitors, namely SP600125 (SP), SB203580 (SB), and U0126 (U), which inhibit JNK, P38, and ERK, respectively. The results showed that expression of JNK, P38, and ERK was significantly reduced after inhibitors were added (Supplementary Figure 4A–F). Furthermore, we examined the apoptosis of macrophages in the si-control and si-Irgm1 groups after inhibiting the MAPK pathways (Figure 6D). In both the si-control and si-Irgm1 intra-group analyses, compared with the untreated group, the expression of Bax, cleaved-caspase3, and cleaved-caspase9 in the ox-LDL-treated group was significantly increased, while the expression of Bcl2 was decreased (Figure 6D Lane 1 vs. 2; Lane 6 vs. 7; Figure 6E–H). After adding SP600125, SB203580, and U0126, the expression of Bax, cleaved-caspase3, and cleaved-caspase9 were significantly reduced, in contrast with the increased expression of Bcl2 (Figure 6D, lane 3–5 vs. lane 2; Lane 8–10 vs. lane 7; Figure 6H). Taken together, these results show that Irgm1 can induce ROS production, which subsequently activates the MAPK signaling pathways and leads to apoptosis in macrophages.

Irgm1 aggravates plaque progression in bone marrow chimera recipient mice and

contributes to macrophage apoptosis. Next, we investigated by use of bone marrow chimera recipient mice whether Irgm1 expressed on hematopoietic origin cells contributes to atherosclerosis progression. Mouse donor cells from ApoE$^{-/-}$Irgm1$^{+/+}$ or ApoE$^{-/-}$Irgm1$^{+/-}$ mice were transplanted into ApoE$^{-/-}$Irgm1$^{+/-}$ mice (Figure 7A). We first assessed the cholesterol crystals in the plaques in the aortic sinus using laser reflection microscopy and found that there was a reduced amount of cholesterol crystals in ApoE$^{-/-}$Irgm1$^{+/-}$ mice plaques (Figure 7B–C). H&E staining was used to observe and measure the necrotic core area, fibrous cap thickness (FCT), and plaque area. The results showed that compared with ApoE$^{-/-}$Irgm1$^{+/+}$ mice, the fibrous cap in the plaque of ApoE$^{-/-}$Irgm1$^{+/-}$ mice was thicker, and the necrotic core area, ratio, and plaque area were significantly reduced (Figure 7D–7E, 7H, Supplemental Figure 7A). ORO staining was used to observe the neutral lipids of aortic sinus plaques and we found that the ratio of neutral lipids in ApoE$^{-/-}$Irgm1$^{+/-}$ mice plaques was reduced (Figure 7F, 7I). We then observed the collagen fibers of aortic sinus plaques by Masson staining. Compared with ApoE$^{-/-}$Irgm1$^{+/+}$ mice, both the content and ratio of collagen fibers in the plaques of ApoE$^{-/-}$Irgm1$^{+/-}$ mice showed a significant reduction (Figure 7G, 7J; Supplemental Figure 7C). All these results were consistent with those in non-recipient mice outlined in Figure 3. Overall, Irgm1 aggravates plaque progression in bone marrow chimera recipient mice.

To further verify the relationship between Irgm1 and apoptosis in macrophages, we detected the expression of cleaved-caspase3 and cleaved-caspase9 in the aortic sinus

by immunohistochemistry. The results suggested that compared with ApoE$^{-/-}$Irgm1$^{+/+}$ mice, the ratio of cleaved-caspase3 and cleaved-caspase9 in the plaques of ApoE$^{-/-}$ Irgm1$^{+/-}$ mice was significantly reduced (Figure 7K–7N), which was in line with the results at the protein level examined by western blotting (Figure 7O–7Q). Finally, we observed by immunofluorescence the co-localization of cleaved-caspase3 and cleaved-caspase9 with CD68 (Supplemental Figure 5D–5E). In summary, Irgm1 aggravates plaque progression and contributes to apoptosis in macrophages, both in bone marrow chimera recipient and non-chimera mice.

Discussion

Our data confirmed that in the STEMI cohort, serum IRGM levels were high in patients with culprit PR (Figure 2B), which can potentially provide a tool with which to predict PR in patients with STEMI. When adjusted for age, smoking, hypertension, diabetes, serum lipid profile, and other risk factors related to ACS, IRGM was still correlated with PR (Figure 2C). Apparently, IRGM/Irgm1 plays a role in the progression of atherosclerosis. However, the exact mechanism by which IRGM/Irgm1 affects the development of atherosclerotic plaques was unclear. IRGM/Irgm1 is widely expressed in the endoplasmic reticulum and Golgi bodies of macrophages. Macrophages, which are the principal immune cells in plaques, can release many cytokines and subsequently lead to apoptosis, which makes atherosclerotic plaques vulnerable (30, 31). Within this context, it seems natural to assume that IRGM/Irgm1 can change the phenotype of advanced atherosclerotic plaques by affecting the apoptosis of macrophages. Here, we further clarified the exact mechanisms by which Irgm1 affects plaque progression *in vivo* and *in vitro*. Irgm1 is capable of activating the MAPK signaling pathway by promoting ROS production, leading to macrophage apoptosis and, thus, affecting plaque stability (Figure 8). Taken together, these data identify a crucial role for Irgm1 in mediating apoptosis of macrophages during the progression of atherosclerosis, and highlight the power of IRGM as a potential predictor of atherosclerotic plaque vulnerability.

In the 1980s, a post-mortem study conducted by Davies *et al*. showed that PR caused the majority of fatal myocardial infarctions (32). This discovery introduced the concept of vulnerable plaque, which is characterized by a thin fibrous cap, a large area of lipid core, and abundant inflammatory cell infiltration (33). In time, it gave birth to a widely accepted insight that the instability of coronary atherosclerosis is due to the weakening of the collagen structure caused by the inflammatory infiltration and the fissure of TCFA plaques (34). By virtue of its high resolution, intracoronary OCT can not only evaluate the extent of stenosis of the lumen, but also provide accurate information about the anatomical structure of the coronary arteries and observe subtle changes on the intimal side of the vessels (35). The emergence of OCT makes it possible to track the pathogenesis of ACS in patients *in vivo* and assess the morphological features of vulnerable plaques. Our research group has previously discovered *in vivo* that most of the plaques that tend to rupture have thin fibrous caps and large lipid arcs, as assessed by OCT combined with intravascular ultrasound (7). In this study, we compared the morphological characteristics between ruptured and non-ruptured culprit plaques in patients with STEMI. We confirmed that the fibrous cap was thinner and that the proportion of lipid-rich plaque was higher in the group with ruptured plaques (Figure 2A). Thus, there is an imperative to research in depth the pathways leading to progression of atherosclerosis, and to search for biological predictors of PR in patients with ACS. This is necessary to provide precise guidance for prompt detection of vulnerable plaques, as well as to develop individualized treatment strategies.

The pioneer of atherosclerotic inflammation theory, Peter Libby, pointed out very early that inflammation starts from the recruitment of white blood cells and secretion of pro-inflammatory factors in the early stage of atherosclerosis and is involved in the entire process of the disease (36). The CANTOS study published in 2017 revealed that the administration of IL-1β monoclonal antibody canakinumab could provide a significant 15% reduction in the risk of further MI, stroke, or death in those patients with a history of myocardial infarction and C-reactive protein > 2 mg/dL, compared with standard drug therapy. This clinical trial directly proved for the first time the effectiveness of anti-inflammatory treatment on atherosclerotic diseases (37). Thus, inflammation plays an essential role in the progression from vulnerable to ruptured plaque, which ultimately leads to clinical events. Hunn *et al*. have shown that immunity-related GTPases M (IRGM) belong to the family of interferon-induced GTPases (IRGs) and are one of the most potent cell-autonomous resistance systems for intracellular pathogens (38). IRGM is genetically and functionally related to a variety of proteins implicated in chronic inflammatory diseases (39). Therefore, we detected the expression of serum IRGM in patients with STEMI and found that serum IRGM was significantly higher in the RUP group (Figure 2B). Haddy *et al*. emphasized that TNF-α induces the production of IL-6 and the adhesion of leukocytes to the endothelium. IL-6, an upstream inflammatory cytokine, plays a central role in the spread of downstream inflammatory responses that lead to atherosclerosis (40). Consequently, we quantified the expression of serum

IRGM, IL-6, and TNF-α, and found that expression of IRGM was positively correlated with IL-6 and TNF-α (Supplemental Figure 2D–G). These findings indicate that IRGM/Irgm1 plays a potential role in the progression of atherosclerosis.

In previous studies, IRGM/Irgm1 was found to play a critical role in IFN-γ-induced autophagy (41, 42). It has been reported that IRGM/Irgm1 can promote macrophage autophagy and inhibit the activation of inflammasome NLRP3, thereby protecting the intestine from inflammatory attack (39, 43). Human IRGM proteins are widely targeted by RNA viruses, some of which, such as the hepatitis C virus or measles virus, can improve their own replication ability by autophagy in human cells (44, 45). In addition, Yang *et al*. found that using microRNA to inhibit the expression of IRGM/Irgm1 can directly or indirectly attenuate the autophagy of macrophages induced by the peste des petits ruminants virus (46). Hence, IRGM/Irgm1 is known as an autophagy-related protein and has been widely studied in inflammation and tumor diseases. However, there are few studies on IRGM/Irgm1 in the area of cardiovascular disease. In the present study, we confirmed that IRGM was highly expressed in the RUP group, which was related to the vulnerability of advanced atherosclerotic plaques (Figure 2D). We next asked whether IRGM/Irgm1 can aggravate the progression of atherosclerotic plaques by influencing macrophage autophagy. In this study, after stimulating the RAW264.7 macrophage cell line by ox-LDL *in vitro* for 3 h, we detected autophagic indicators LC3, P62, Atg5, and beclin1 at mRNA and protein levels, and found that

Irgm1 can indeed promote macrophage autophagy. Moreover, we used mRFP-GFP tandem fluorescent-tagged LC3II to examine autophagosome–lysosome fusion. RFP-positive/GFP-negative puncta are indicative of fusion. Treatment with si-Irgm1 increased RFP-positive/GFP-positive puncta, suggesting that si-Irgm1 inhibits autophagosome–lysosome fusion (Supplemental Figure 1). Therefore, we speculate that in the early stage of atherosclerosis, Irgm1 may prevent plaque progression by promoting autophagy in macrophages. However, after stimulating the RAW264.7 macrophage cell line with ox-LDL for 48 h, we were disappointed to find that regardless of the presence of Irgm1, we could only observe RFP-positive/GFP-positive puncta. These results suggest that the autophagy flux of macrophages in an advanced atherosclerotic model is blocked (Supplemental Figure 1). Therefore, the effect of IRGM on macrophage autophagy cannot be used to explain the changes in plaque vulnerability in advanced atherosclerosis.

Much evidence has accrued that the apoptosis of macrophages can influence the stability of atherosclerotic plaques (25, 47). Macrophage apoptosis intensifies the formation of plaque necrotic cores, causes thinning of the fibrous cap, and ultimately leads to PR (48-50). Therefore, we speculate that IRGM/Irgm1 contributes to plaque vulnerability by promoting macrophage apoptosis in advanced atherosclerotic plaques. In this study, we compared the phenotype of advanced atherosclerotic plaques in ApoE$^{-/-}$Irgm1$^{+/+}$ and ApoE$^{-/-}$Irgm1$^{+/-}$ mice *in vivo* and found that ApoE$^{-/-}$Irgm1$^{+/-}$ mice have a

smaller aortic plaque area, and a reduction in cholesterol crystals, necrotic core, and neutral lipids. In contrast, the collagen fiber content is higher, which indicates that Irgm1 can aggravate the progression of advanced atherosclerotic plaques (Figure 3). Next, we evaluated the macrophage apoptosis-related proteins cleaved-caspase3 and cleaved-caspase9 and found that Irgm1 can promote macrophage apoptosis (Figure 4). These findings were also confirmed *in vitro*. Finally, bone marrow transplantations of ApoE$^{-/-}$ mice reconstituted with either ApoE$^{-/-}$Irgm1$^{+/+}$ or ApoE$^{-/-}$Irgm1$^{+/-}$ mice bone marrow indicates that Irgm1 deficiency in bone marrow-derived cells can significantly delay the progression of atherosclerosis and stabilize plaques (Figure 7). Nevertheless, we do not know the exact mechanisms by which Irgm1 can affect macrophage apoptosis. Various hypotheses have been proposed to explain the apoptosis of macrophages in advanced atherosclerosis, such as deprivation of growth factors or the presence of toxic cytokines (51, 52), yet there is no evidence for these hypotheses *in vivo*. Several studies have pointed out that an increased accumulation of ROS, the product of endoplasmic reticulum stress, activates MAPK, which in turn causes the release of the mitochondrial pro-apoptotic proteins caspase3/7/9, subsequently leading to cell apoptosis (53, 54). Several lines of evidence suggest that endoplasmic reticulum stress may significantly promote the apoptosis of macrophages in advanced plaques (55, 56). In the current study, we used immunofluorescence and flow cytometry to detect reactive oxygen fluorescent probes *in vitro* and found that Irgm1 can promote ROS production in macrophages. Interestingly, when we treated Raw264.7 cell line with the ROS

scavenger NAC with the aim of silencing Irgm1, the amounts of apoptosis-related proteins cleaved-caspase3 and cleaved-caspase9 sharply decreased. These results suggest that Irgm1 can lead to apoptosis *in vitro* by promoting ROS production in macrophages. Prior studies have successfully detected the markers of endoplasmic reticulum stress and macrophage apoptosis in human atherosclerotic plaques, which further confirmed the reliability of our data in the present study. In summary, these findings lay the foundation for our next exploration of the exact apoptotic signaling pathways of Irgm1 through endoplasmic reticulum stress.

It has been well established that ROS can induce autophagy. In turn, autophagy depletes damaged mitochondria (the primary source of ROS), thereby reducing ROS production. This "circle" represents a fine-tuned negative feedback mechanism. Through this mechanism, autophagy eliminates the source of oxidative stress and protects cells from oxidative damage (57, 58). However, with the continuous accumulation of ROS inside the cells, depolarization of the inner mitochondrial membrane is triggered. These depolarized mitochondria become fragmented and eventually lead to cell apoptosis (48, 59). Collectively, these studies outline a critical role for ROS in the two independent and interactive signaling pathways of apoptosis and autophagy. In the past ten years, many studies have explored the relationship between autophagy and apoptosis. Interestingly, molecules that incipiently play a role in one pathway may also participate in another pathway. Previous studies have shown that both autophagy and apoptosis

respond to the same stimulus (ROS) and share the key regulatory protein MAPK (54, 60). The MAPK signaling pathway is regulated by ERK1/2, c-Jun N-terminal kinase1/2/3 (JNK1/2/3), and p38-MAPK in the processes of cell differentiation, autophagy, apoptosis, and inflammation (61, 62). Therefore, we speculate that Irgm1 promotes ROS production in macrophages and activates apoptosis via the MAPK signaling pathway. In this study, we verified that Irgm1 could activate the MAPK signaling pathway through ROS. Compared with the control group, when macrophages were treated with ERK1/2, JNK, and p38-MAPK inhibitors, the expression of the apoptotic proteins BAX, Bcl-2, *cleaved-caspase*3, and *cleaved-caspase*9 were significantly reduced (Figure 6). In summary, these results indicate that Irgm1 can activate the MAPK signaling pathway and cause macrophage apoptosis.

The generalizability of these results is subject to certain limitations. First, as a retrospective study, the clinical data reflect the current epidemiological, serum, and plaque features of Chinese patients with STEMI. Therefore, it may not be generalizable to patients with NSTE-ACS or patients from other countries or regions. Second, although there is a definition of macrophage infiltration in a published consensus on OCT, it remains a controversial topic to recognize macrophage infiltration by OCT. Therefore, this study did not list the data of macrophage infiltration by OCT between the RUP and NO-RUP groups. Third, as it is not possible for us to obtain the coronary arteries from clinical patients, our research group used lower limb arteries obtained

from vascular surgery to assess plaque characteristics, which may not accurately reflect the profile of coronary plaques. Fourth, since ApoE$^{-/-}$Irgm1$^{-/-}$ mice with the background of C57BL/6 may be embryonic lethal, we have hitherto been unable to obtain the above double-gene knockout mice. Thus, in the present study, we were only able to use ApoE$^{-/-}$Irgm1$^{+/-}$ mice as the experimental group *in vivo*. Fifth, it may be of vital importance to study the progression of atherosclerotic plaques by establishing an atherosclerosis model through a high-fat diet. However, this modeling method may not be representative for the study of PR. In response, we are actively seeking a way to construct a PR model to compensate for the drawback of this research. Based on the conclusions we have made so far, we have abundant reasons to believe that Irgm1 is a suitable predictive factor for rupture in the rupture model of advanced atherosclerotic mice. Sixth, our research found that Irgm1 regulates macrophage apoptosis by activating the MAPK signaling pathway. A minor objection is that we and other research groups have not yet verified the specific site at which Irgm1 acts in regulating the MAPK signaling pathway. Seventh, studies have confirmed that the in sequence of IRGM (+313) (rs10065372), an SNP is present at position +313 inside exon 2 of IRGM in chromosome 5q33.1. This SNP is associated with severe sepsis that has a high fatality rate. However, it is not clear whether mouse Irgm1 also has the same sequence as human IRGM. Therefore, for this *in vivo* study, we did not target to silence the specific sequence of Irgm1. We silenced Irgm1 by non-specific liposome transfection, keeping its silencing efficiency between 70 and 80%. Overall, although we must keep in mind

these limitations in the present study, we are confident in the credibility of our findings due to the multiplicity of approaches taken, all of which reinforce each other.

In conclusion, the relevance of IRGM and PR in patients with STEMI is for the first time clearly supported by the current findings. Additionally, IRGM may become a potiential predictor of PR in patients with STEMI. *In vivo* experiments further confirmed that Irgm1 aggravates the progression of atherosclerotic plaques by promoting macrophage apoptosis, which is induced by the production of ROS and subsequent activation of the MAPK signaling pathway. Our data reveal the molecular mechanisms underlying these effects and pinpoint IRGM/Irgm1 as a potential target for anti-atherosclerotic therapies.

Methods

Study Participants. In this study, 135 patients who were diagnosed with STEMI in the 2nd Affiliated Hospital of Harbin Medical University (Harbin, China) between August 2016 and December 2016 and who underwent OCT after thrombus aspiration were enrolled. The main exclusion criteria were angina pectoris, myocarditis, heart failure, aortic dissection, acute and chronic infections and infectious diseases, liver and kidney insufficiency, and severe progressive diseases. We finally enrolled 85 patients with STEMI. We divided patients into two groups: patients with PR (RUP group) (n=52) and without PR (NO-RUP group) (n=33). Eight additional healthy volunteers were also recruited. Subsequently, we analyzed OCT images and obtained the serum of these 85 patients and 8 healthy volunteers. The definition of STEMI was in accordance with the 2015 ACC/AHA/SCAI guidelines published previously (63).

OCT Image Acquisition and analysis. The frequency-domain OCT ILUMIEN system, along with the Dragon fly catheter (St. Jude Medical, Westford, Massachusetts, USA) were used to acquire OCT imaging of culprit lesions, as shown previously (9). Two experienced independent investigators (H.C and S.S) analyzed OCT images according to the criteria of the Consensus OCT Document (64) using a proprietary OCT review workstation (St. Jude Medical, Westford, MA, USA) at intravacular imaging and physiology core lab. In the case of discordance between these two observers, there was

a consensus reading obtained by judgement with another investigator. All investigators were blinded to the subject information. Plaque rupture was defined as a lipid plaque with fibrous cap continuity destroyed plus a clear cavity formation within the plaque. The FCT covering the lipid core was measured three times at the thinnest location, and the mean value of triplicate measurements was worked out. TCFA was a lipid plaque in the presence of FCT <65 μm with a maximum lipid arc of at least 90° (65).

Patient blood vessel specimens. All atherosclerotic middle artery vessels were obtained from patients with arterial occlusion in the Department of Vascular Surgery of the First Affiliated Hospital of Harbin Medical University, and all normal vessels were obtained from five patients who underwent lower limb amputation. Blood vessel specimens from all patients were transported to the laboratory by dry ice and maintained at low temperature (−40 °C) after being isolated. All blood vessel specimens were embedded in paraffin and sectioned consecutively (4 μm) for H&E and immunohistochemical staining.

Animals. Irgm1$^{-/-}$ mice (C57B/L6 background) were derived from a published source (17). Irgm1$^{-/-}$ mice and ApoE$^{-/-}$ mice were crossed to obtain ApoE$^{+/-}$Irgm1$^{+/-}$ mice. We then screened ApoE$^{-/-}$Irgm1$^{+/-}$ mice by crossing ApoE$^{+/-}$Irgm1$^{+/-}$ mice. Due to the probability of embryonic lethality in ApoE$^{-/-}$Irgm1$^{-/-}$ mice, we genetically identified

offspring of ApoE$^{-/-}$Irgm1$^{+/-}$ mice crossed with ApoE$^{-/-}$Irgm1$^{+/-}$ mice. After genotyed by PCR, we then established a model of advanced atherosclerosis in mice by high-fat diet for sixteen weeks.

Reagents. See Supplemental Table 3–4.

Bone marrow chimera recipient mice. We fed ApoE$^{-/-}$Irgm1$^{+/+}$ (6–8 weeks old) recipient mice with fradiomycin and polymyxin, supplemented with sterile pH 3.0 water for a week, and then irradiated them with 9 Gy of radiation.

Next, we divided the recipient mice into three groups. Bone marrow macrophages (5×10^6) from ApoE$^{-/-}$Irgm1$^{+/+}$ donor mice and ApoE$^{-/-}$Irgm1$^{+/-}$ donor mice were reinfused into two groups of recipient mice by tail vein injection, plus the last group was left untreated to become a control group. After about seven days, the mice from the control group died and the ones from experimental group survived normally, indicating that the modeling was successful. We then started to provide a high-fat diet for 16 weeks to establish a late AS model.

Cell culture. We cultured Raw264.7 cells in Dulbecco's Modified Eagle's medium (DMEM) (SH30022.01B, HYCLONE, USA) containing 10% FBS (0500, ScienCell,

USA). Cells were seeded in 60 mm dishes or 6- and 12-well plates. We use above cells after they grew to 60%–80% confluence.

Transfection. We seeded cells in 6- and 24-well plates and when they reached 70–80% confluence, the knockdown of Irgm1(5'-GGGCUGGGAUUCUGUCAUA-3') or a negative control (5'-CGUACGCGGAAUACUUCGAUU-3') was obtained by transfection with siRNA (GenePharma, Shanghai, China) and Lipo3000 (L3000008, Invitrogen, USA) using FBS-free DMEM medium. After 6–8 h of transfection, the transfection was continued for 24 h with 10% DMEM. Real-time quantitative PCR was utilized to confirm the efficiency of transfection.

ROS detection. The generation of ROS after ox-LDL treatment in cells was evaluated by the fluorescence intensity of the dihydroethidium (DHE) probe. After the intake of ox-LDL, macrophages were harvested, washed, and then incubated with 5 μM DHE probe (S0063, Beyotime, China) for 30 min at 37 °C, protected against exposure to light. After rinsing, fluorescent signals were immediately measured using a fluorescence microscope and FACS Verse flow cytometer (BD, USA).

Real-time quantitative PCR (RT-qPCR). Total RNA was extracted by Trizol reagent

(ThermoFisher, USA) and reverse-transcribed utilizing the RT Easy II First Strand cDNA Synthesis Kit (04379012001, Roche, Switzerland). Then, we amplified cDNA (18 ng) in a Real-Time PCR Easy (SYBR Green I) (HY-K0501, MCE, China) on Bio-RAD Sequence Detection system (Bio-RAD, USA). The following primers were used: Atg5, forward 5'-CTTCTGCACTGTCCATCTAAGG-3' and reverse, 5'-ATCCAGAGTTGCTTGTGATCTT-3'; Atg7, forward 5'-GCAGCCAGCAAGCGAAAG-3' and reverse, 5'-CCGGTCTCTGGTTGAATCTCCTG-3'; Beclin 1, forward 5'-CCCGTGGAATGGAATGAGATTA-3' and reverse, 5'-CCGTAAGGAACAAGTCGGTATC-3'; LC3, forward 5'-AGAGTGGAAGATGTCCGGCT-3' and reverse, 5'-CACTTCGGAGATGGGAGTGG-3'. Gene expression values were normalized against that of β-actin.

Pathological staining. We placed hearts in a mold containing a tissue-freezing medium, which was perfused with PBS and frozen. Eight μm-thick (H&E staining) and twenty μm-thick (ORO staining) sections were cut from the hearts, from caudal of the aortic sinus to the proximal aorta. Slides were fixed with 4% paraformaldehyde and then stained. Methods of H&E, ORO, and Masson staining are as previously described (17).

Immunofluorescence. Frozen slides were rewarmed at RT for 10 min. Next, slides were fixed with cold acetone (−20 °C) for another 10 min. The slides were then rinsed in distilled water for 5 min three times each. Subsequently, we incubated slides with 0.3% Triton-X 100 membrane breaker for 30 min at 37 °C , and incubated with the primary antibody at 4 °C overnight. On the second day, frozen slides were rewarmed for 10 min at room temperature (RT), followed by rinsing in distilled water three times for 5 min each. Next, we incubated frozen slides with secondary antibody at RT for 1 h. The slides were rinsed in distilled water three times for 5 min each. Finally, DAPI was added and images were captured using a confocal laser scanning microscope (ZEISS LSM 700).

Immunohistochemistry. Frozen slides were rewarmed at RT for 10 min and then fixed with cold acetone (−20 °C) for another 10 min. After rinsed in distilled water three times for 5 min each, slides were incubated with 0.3% Triton-X 100 rupture solution at 37 °C for 30 min. Then, we blocked endogenous peroxidase with 3% hydrogen peroxide, and slides were incubated with primary antibody at 4 °C overnight. On the next day, frozen slides were rewarmed for 10 min at RT and then rinsed in distilled water three times for 5 min each. Slides were incubated with secondary antibody at RT for 1 h. Next, slides were rinsed in distilled water for three times for 5 min each, then exposed to 3,3'-diaminobenzidine (DAB) (ZSGQ-BIO, China) stain for 1–10 min, followed by Hematoxylin stain. Images were taken by ordinary forward microscopy (Olympus, BX41). Paraffin sections were first dewaxed and then fixed with 4% PFA for 5 min.

After rinsing with PBS, the sections were incubated with 0.3% Triton-X 100 membrane breaking solution at 37 °C for 30 min, then antigen repair was proceeded. The rest of the steps were the same as for frozen sections.

Western blot analysis. We lysed cells in radioimmunoprecipitation assay (RIPA) buffer on ice, adding protease and phosphatase inhibitors. Then we obtained nuclear and cytosolic fractions using a nuclear/cytosol fractionation kit (R0050, Solarbio, China). Total protein was extracted with RIPA buffer together with phenylmethylsulfonyl fluoride, as well as Halt Protease and Phosphatase Inhibitor. The protein concentration was measured by a bicinchoninic acid protein assay. We separated 30 μg protein samples by sodium dodecyl sulfate-polyacrylamide gel electrophoresis (SDS-PAGE, P0015, Beyotime, China) and then they were transferred to 0.22-μm PVDF membranes. After blocking with 5% dried skimmed milk for 2 h at RT in Tris-buffered saline, the membranes were probed with primary antibodies (1:1000) and incubated overnight at 4 °C. Next, the membranes were incubated for 2 h in the presence of horseradish peroxidase (HRP)-conjugated secondary antibodies (1:8000) at RT. Chemiluminescence was utilized to visualized immunoreactivity by a ChemiDoc™ MP Imaging System (Tanon, China). We quantified the bands of proteins on the blots by a Bio-Rad Chemi EQ densitometer and Bio-Rad Quantity One software (Tanon, China) and normalized to GAPDH.

ELISA. Before the standard was prepared, we first placed the ELISA kit at RT for 30 min. Next, we added HRP-conjugate reagent (100 μL) / well and incubated each well at 37 °C for 1 h. Subsequently, wash solution (300 μL) / well was added for cleaning, allowed to stand for 1 min, before discarding and repeating four times. Next, we added a total of 50 μL of chromogen solution A and B to each well, and incubated at 37 ° for 15 min without light. The reactions were stopped after adding 50 μL of stop solution to each well. The OD value was finally detected using the enzyme labeling instrument (TECAN, M200pro).

Genotyping. Excised mouse toes were placed into 1.5 mL microcentrifuge tubes, to which was added 100 μL tissue digestion solution (bimake). The tubes were digested in a 55 °C metal bath for 15 min, and then incubated in a 95 °C metal bath for 5 min to inactivate the enzymes in the digestion solution. We centrifuged tubes at 12,000 rpm for 5 min. Then, we use the supernatant (1000 ng) as the PCR template. The primer sequences were LRG1 5'-GGAGAAAGTGAAGTACCC-3'; LRG2 5'-CTCTGACACCGAGAGAAT-3'; Neo3 5'-CATTTGTCACGTCCTGCA-3'. Next, PCR amplification was performed, followed by agarose gel electrophoresis and imaging analysis using a gel imaging system (BIO RAD, GelDoc Go).

Autophagy with double-labeled adenovirus. Raw264.7 cells were inoculated in confocal dishes and grown to 60%–80% confluency before being used the next day for transfection with si-Irgm1. After 8 h, cultures were changed to 10% DMEM, transfection continued for 24 h. Solution was changed on the third day, and replaced with serum-free DMEM (500 μL) in a confocal dish. Adenovirus (1.5 μL) was added, and cells were transfected for 3 h in 10% DMEM. Finally, ox-LDL was added, and transfection continued for 3 h or 48 h. We captured the images by a confocal laser scanning microscope (ZEISS LSM 700).

Flow cytometry. Apoptosis of the cells was detected by Annexin V-fluorescein isothiocyanate (FITC)/PI double staining. Next, in a 5% CO2 incubator, we cultured cells for 48 h at 37 °C. Centrifuging and resuspending of the cells were performed in the binding buffer (200 μL), before reacting with Annexin V-FITC (ab14085, Abcam Inc., Cambridge, MA, USA) (10 μL) and PI (5 μL). Reaction proceeded against the light for 15 min. Finally, binding buffer (300 μL) was added to the cell samples. We used ACS Verse flow cytometer (BD, USA) at an excitation wavelength of 488 nm to detect cell apoptosis.

Statistics. Statistical analyses were performed using SPSS version 20.0 (SPSS, Inc., Chicago, IL, USA) or GraphPad Prism 7.0 (GraphPad Software). Continuous variables

were expressed as mean ± SD for normally distributed variables and as median (25, 75th percentiles) for non-normally distributed variables, and assessed by Student *t-test* or Mann-Whitney U test, respectively. Categorical variables were presented as counts and percentages, and the comparisons were performed using a Chi-square test or Fisher's exact-test. A series of multiple logistic regression models were used to assess the relationship between the risk of plaque rupture and plasma IRGM levels. A 2-sided p value <0.05 was considered statistically significant. All data were analyzed by an independent statistician.

Study approval. This study was approved by the Ethics Committee of the 2nd Affiliated Hospital of Harbin Medical University (Harbin, China), and all patients provided written informed consent. All animals were sacrificed by cervical dislocation. Animal experiments were performed according to guidelines approved by the Institutional Animal Care Committee and in compliance with the guidelines from Directive 2010/63/EU of the European Parliament with approval from the Harbin Medical University Ethics Review Board.

Author contributions

SHF, SS, HXC, BS, and BY designed the experiments. HXC and SS wrote the draft of the manuscript, followed by editing by SHF, YB, and JWT. SS, XRH, XYZ, JTT, ZYL, and ZZH performed the animal experiments; SHF, HXC, XW, SS, CCL, and WH performed experiments *in vitro*. ZMZ and CCL collected all clinical data. HXC, SS, and JWT measured the clinical images. SJW and HXC analyzed and visualized the clinical results. BS and LMY provided crucial reagents. BY, BS, and JWT take responsibility for the accuracy of the analysis of the whole experiment.

Acknowledgments

Dr. Yu was supported by the National Key R&D Program (No. 2016YFC1301100, 2016YFC1301101) and Major Instrument Development Project of the National Natural Science Foundation of China (No. 81827806). Dr. Fang was supported by the National Natural Science Foundation of China (No. 81870353) and the Natural Science Foundation of Heilongjiang Province (No. LH2020H048). The authors thank all the participants and staff from the coronary interventional therapy team and the intravascular imaging core laboratory from the 2nd Affiliated Hospital of Harbin Medical University.

References

1. Libby P, and Hansson GK. Inflammation and immunity in diseases of the arterial tree: players and layers. Circ Res. 2015;116(2):307-11.
2. Libby P. Current concepts of the pathogenesis of the acute coronary syndromes. Circulation. 2001;104(3):365-72.
3. Virmani R, Kolodgie FD, Burke AP, Farb A, and Schwartz SM. Lessons from sudden coronary death: a comprehensive morphological classification scheme for atherosclerotic lesions. Arterioscler Thromb Vasc Biol. 2000;20(5):1262-75.
4. Naghavi M, Libby P, Falk E, Casscells SW, Litovsky S, Rumberger J, et al. From vulnerable plaque to vulnerable patient: a call for new definitions and risk assessment strategies: Part I. Circulation. 2003;108(14):1664-72.
5. Higuma T, Soeda T, Abe N, Yamada M, Yokoyama H, Shibutani S, et al. A Combined Optical Coherence Tomography and Intravascular Ultrasound Study on Plaque Rupture, Plaque Erosion, and Calcified Nodule in Patients With ST-Segment Elevation Myocardial Infarction: Incidence, Morphologic Characteristics, and Outcomes After Percutaneous Coronary Intervention. JACC Cardiovasc Interv. 2015;8(9):1166-76.
6. Jia H, Abtahian F, Aguirre AD, Lee S, Chia S, Lowe H, et al. In vivo diagnosis of plaque erosion and calcified nodule in patients with acute coronary syndrome by intravascular optical coherence tomography. J Am Coll Cardiol. 2013;62(19):1748-58.

7. Tian J, Ren X, Vergallo R, Xing L, Yu H, Jia H, et al. Distinct morphological features of ruptured culprit plaque for acute coronary events compared to those with silent rupture and thin-cap fibroatheroma: a combined optical coherence tomography and intravascular ultrasound study. J Am Coll Cardiol. 2014;63(21):2209-16.

8. Burke AP, Farb A, Malcom GT, Liang YH, Smialek J, and Virmani R. Coronary risk factors and plaque morphology in men with coronary disease who died suddenly. N Engl J Med. 1997;336(18):1276-82.

9. Dai J, Xing L, Jia H, Zhu Y, Zhang S, Hu S, et al. In vivo predictors of plaque erosion in patients with ST-segment elevation myocardial infarction: a clinical, angiographical, and intravascular optical coherence tomography study. Eur Heart J. 2018;39(22):2077-85.

10. Kang SJ, Mintz GS, Weisz G, Mehran R, Rabbani LE, Verheye S, et al. Age-related effects of smoking on coronary artery disease assessed by gray scale and virtual histology intravascular ultrasound. Am J Cardiol. 2015;115(8):1056-62.

11. Dai J, Xing L, Hou J, Jia H, Hu S, Tian J, et al. Chronic kidney disease predicts coronary plaque vulnerability: an optical coherence tomography study. Coron Artery Dis. 2017;28(2):135-44.

12. MacMicking JD, Taylor GA, and McKinney JD. Immune control of tuberculosis by IFN-gamma-inducible LRG-47. Science. 2003;302(5645):654-9.

13. Hunn JP, Koenen-Waisman S, Papic N, Schroeder N, Pawlowski N, Lange R,

et al. Regulatory interactions between IRG resistance GTPases in the cellular response to Toxoplasma gondii. EMBO J. 2008;27(19):2495-509.

14. Rogala AR, Schoenborn AA, Fee BE, Cantillana VA, Joyce MJ, Gharaibeh RZ, et al. Environmental factors regulate Paneth cell phenotype and host susceptibility to intestinal inflammation in Irgm1-deficient mice. Dis Model Mech. 2018;11(2).

15. Tian L, Li L, Xing W, Li R, Pei C, Dong X, et al. IRGM1 enhances B16 melanoma cell metastasis through PI3K-Rac1 mediated epithelial mesenchymal transition. Sci Rep. 2015;5:12357.

16. Xia F, Li R, Wang C, Yang S, Tian L, Dong H, et al. IRGM1 regulates oxidized LDL uptake by macrophage via actin-dependent receptor internalization during atherosclerosis. Sci Rep. 2013;3:1867.

17. Fang S, Xu Y, Zhang Y, Tian J, Li J, Li Z, et al. Irgm1 promotes M1 but not M2 macrophage polarization in atherosclerosis pathogenesis and development. Atherosclerosis. 2016;251:282-90.

18. Wang W, Liu W, Fidler T, Wang Y, Tang Y, Woods B, et al. Macrophage Inflammation, Erythrophagocytosis, and Accelerated Atherosclerosis in Jak2 (V617F) Mice. Circ Res. 2018;123(11):e35-e47.

19. Kasikara C, Doran AC, Cai B, and Tabas I. The role of non-resolving inflammation in atherosclerosis. J Clin Invest. 2018;128(7):2713-23.

20. Hasegawa H, Watanabe T, Kato S, Toshima T, Yokoyama M, Aida Y, et al. The

role of macrophage transcription factor MafB in atherosclerotic plaque stability. Atherosclerosis. 2016;250:133-43.

21. Colin S, Chinetti-Gbaguidi G, and Staels B. Macrophage phenotypes in atherosclerosis. Immunol Rev. 2014;262(1):153-66.

22. Sun W, Lin Y, Chen L, Ma R, Cao J, Yao J, et al. Legumain suppresses OxLDL-induced macrophage apoptosis through enhancement of the autophagy pathway. Gene. 2018;652:16-24.

23. Tajbakhsh A, Kovanen PT, Rezaee M, Banach M, Moallem SA, and Sahebkar A. Regulation of efferocytosis by caspase-dependent apoptotic cell death in atherosclerosis. Int J Biochem Cell Biol. 2020;120:105684.

24. Wu Y, Zhang Y, Dai L, Wang Q, Xue L, Su Z, et al. An apoptotic body-biomimic liposome in situ upregulates anti-inflammatory macrophages for stabilization of atherosclerotic plaques. J Control Release. 2019;316:236-49.

25. Wang D, Wang W, Lin W, Yang W, Zhang P, Chen M, et al. Apoptotic cell induction of miR-10b in macrophages contributes to advanced atherosclerosis progression in ApoE-/- mice. Cardiovasc Res. 2018;114(13):1794-805.

26. Fleiner M, Kummer M, Mirlacher M, Sauter G, Cathomas G, Krapf R, et al. Arterial neovascularization and inflammation in vulnerable patients: early and late signs of symptomatic atherosclerosis. Circulation. 2004;110(18):2843-50.

27. Tabas I. Macrophage death and defective inflammation resolution in atherosclerosis. Nat Rev Immunol. 2010;10(1):36-46.

28. Assolini JP, Tomiotto-Pellissier F, da Silva Bortoleti BT, Goncalves MD, Sahd CS, Carloto ACM, et al. Diethyldithiocarbamate encapsulation reduces toxicity and promotes leishmanicidal effect through apoptosis-like mechanism in promastigote and ROS production by macrophage. J Drug Target. 2020;28(10):1110-23.

29. Mi Y, Xiao C, Du Q, Wu W, Qi G, and Liu X. Momordin Ic couples apoptosis with autophagy in human hepatoblastoma cancer cells by reactive oxygen species (ROS)-mediated PI3K/Akt and MAPK signaling pathways. Free Radic Biol Med. 2016;90:230-42.

30. Larabi A, Barnich N, and Nguyen HTT. New insights into the interplay between autophagy, gut microbiota and inflammatory responses in IBD. Autophagy. 2020;16(1):38-51.

31. Hoseini Z, Sepahvand F, Rashidi B, Sahebkar A, Masoudifar A, and Mirzaei H. NLRP3 inflammasome: Its regulation and involvement in atherosclerosis. J Cell Physiol. 2018;233(3):2116-32.

32. Davies MJ, and Thomas A. Thrombosis and acute coronary-artery lesions in sudden cardiac ischemic death. N Engl J Med. 1984;310(18):1137-40.

33. Falk E, Shah PK, and Fuster V. Coronary plaque disruption. Circulation. 1995;92(3):657-71.

34. Finn AV, Nakano M, Narula J, Kolodgie FD, and Virmani R. Concept of vulnerable/unstable plaque. Arterioscler Thromb Vasc Biol. 2010;30(7):1282-

92.

35. Tearney GJ. Intravascular optical coherence tomography. Eur Heart J. 2018;39(41):3685-6.

36. Libby P. Molecular bases of the acute coronary syndromes. Circulation. 1995;91(11):2844-50.

37. Ridker PM, Everett BM, Thuren T, MacFadyen JG, Chang WH, Ballantyne C, et al. Antiinflammatory Therapy with Canakinumab for Atherosclerotic Disease. N Engl J Med. 2017;377(12):1119-31.

38. Hunn JP, Feng CG, Sher A, and Howard JC. The immunity-related GTPases in mammals: a fast-evolving cell-autonomous resistance system against intracellular pathogens. Mamm Genome. 2011;22(1-2):43-54.

39. Mehto S, Jena KK, Nath P, Chauhan S, Kolapalli SP, Das SK, et al. The Crohn's Disease Risk Factor IRGM Limits NLRP3 Inflammasome Activation by Impeding Its Assembly and by Mediating Its Selective Autophagy. Mol Cell. 2019;73(3):429-45 e7.

40. Haddy N, Sass C, Droesch S, Zaiou M, Siest G, Ponthieux A, et al. IL-6, TNF-alpha and atherosclerosis risk indicators in a healthy family population: the STANISLAS cohort. Atherosclerosis. 2003;170(2):277-83.

41. Amersfoort J, Douna H, Schaftenaar FH, Foks AC, Kroner MJ, van Santbrink PJ, et al. Defective Autophagy in T Cells Impairs the Development of Diet-Induced Hepatic Steatosis and Atherosclerosis. Front Immunol. 2018;9:2937.

42. Liu F, Xue H, Ke J, Wu Y, Yao K, Liang S, et al. Ipr1 Regulation by Cyclic GMP-AMP Synthase/Interferon Regulatory Factor 3 and Modulation of Irgm1 Expression via p53. Mol Cell Biol. 2020;40(8).

43. Mehto S, Chauhan S, Jena KK, Chauhan NR, Nath P, Sahu R, et al. IRGM restrains NLRP3 inflammasome activation by mediating its SQSTM1/p62-dependent selective autophagy. Autophagy. 2019;15(9):1645-7.

44. Gregoire IP, Richetta C, Meyniel-Schicklin L, Borel S, Pradezynski F, Diaz O, et al. IRGM is a common target of RNA viruses that subvert the autophagy network. PLoS Pathog. 2011;7(12):e1002422.

45. Gregoire IP, Rabourdin-Combe C, and Faure M. Autophagy and RNA virus interactomes reveal IRGM as a common target. Autophagy. 2012;8(7):1136-7.

46. Yang B, Xue Q, Guo J, Wang X, Zhang Y, Guo K, et al. Autophagy induction by the pathogen receptor NECTIN4 and sustained autophagy contribute to peste des petits ruminants virus infectivity. Autophagy. 2020;16(5):842-61.

47. Cong G, Yan R, Huang H, Wang K, Yan N, Jin P, et al. Involvement of histone methylation in macrophage apoptosis and unstable plaque formation in methionine-induced hyperhomocysteinemic ApoE(-/-) mice. Life Sci. 2017;173:135-44.

48. Xiao Q, Che X, Cai B, Tao Z, Zhang H, Shao Q, et al. Macrophage autophagy regulates mitochondria-mediated apoptosis and inhibits necrotic core formation in vulnerable plaques. J Cell Mol Med. 2020;24(1):260-75.

49. Yang J, Lin X, Wang L, Sun T, Zhao Q, Ma Q, et al. LncRNA MALAT1 Enhances ox-LDL-Induced Autophagy through the SIRT1/MAPK/NF-kappaB Pathway in Macrophages. Curr Vasc Pharmacol. 2020;18(6):652-62.

50. Wang ZH, Shang YY, Zhang S, Zhong M, Wang XP, Deng JT, et al. Silence of TRIB3 suppresses atherosclerosis and stabilizes plaques in diabetic ApoE-/-/LDL receptor-/- mice. Diabetes. 2012;61(2):463-73.

51. Rusetskaya NY, Fedotov IV, Koftina VA, and Borodulin VB. [Selenium compounds in redox regulation of inflammation and apoptosis]. Biomed Khim. 2019;65(3):165-79.

52. Chen JH, Riazy M, Smith EM, Proud CG, Steinbrecher UP, and Duronio V. Oxidized LDL-mediated macrophage survival involves elongation factor-2 kinase. Arterioscler Thromb Vasc Biol. 2009;29(1):92-8.

53. Su X, Shen Z, Yang Q, Sui F, Pu J, Ma J, et al. Vitamin C kills thyroid cancer cells through ROS-dependent inhibition of MAPK/ERK and PI3K/AKT pathways via distinct mechanisms. Theranostics. 2019;9(15):4461-73.

54. Fan J, Ren D, Wang J, Liu X, Zhang H, Wu M, et al. Bruceine D induces lung cancer cell apoptosis and autophagy via the ROS/MAPK signaling pathway in vitro and in vivo. Cell Death Dis. 2020;11(2):126.

55. Gonzalez L, Qian AS, Tahir U, Yu P, and Trigatti BL. Sphingosine-1-Phosphate Receptor 1, Expressed in Myeloid Cells, Slows Diet-Induced Atherosclerosis and Protects against Macrophage Apoptosis in Ldlr KO Mice. Int J Mol Sci.

2017;18(12).

56. Cominacini L, Garbin U, Mozzini C, Stranieri C, Pasini A, Solani E, et al. The atherosclerotic plaque vulnerability: focus on the oxidative and endoplasmic reticulum stress in orchestrating the macrophage apoptosis in the formation of the necrotic core. Curr Med Chem. 2015;22(13):1565-72.

57. Signorelli S, Tarkowski LP, Van den Ende W, and Bassham DC. Linking Autophagy to Abiotic and Biotic Stress Responses. Trends Plant Sci. 2019;24(5):413-30.

58. Guo QQ, Wang SS, Zhang SS, Xu HD, Li XM, Guan Y, et al. ATM-CHK2-Beclin 1 axis promotes autophagy to maintain ROS homeostasis under oxidative stress. EMBO J. 2020;39(10):e103111.

59. Singh N, Lawana V, Luo J, Phong P, Abdalla A, Palanisamy B, et al. Organophosphate pesticide chlorpyrifos impairs STAT1 signaling to induce dopaminergic neurotoxicity: Implications for mitochondria mediated oxidative stress signaling events. Neurobiol Dis. 2018;117:82-113.

60. Zhang G, He J, Ye X, Zhu J, Hu X, Shen M, et al. beta-Thujaplicin induces autophagic cell death, apoptosis, and cell cycle arrest through ROS-mediated Akt and p38/ERK MAPK signaling in human hepatocellular carcinoma. Cell Death Dis. 2019;10(4):255.

61. Hammouda MB, Ford AE, Liu Y, and Zhang JY. The JNK Signaling Pathway in Inflammatory Skin Disorders and Cancer. Cells. 2020;9(4).

62. Silva SLR, Baliza IRS, Dias RB, Sales CBS, Rocha CAG, Soares MBP, et al. Ru(II)-thymine complex causes DNA damage and apoptotic cell death in human colon carcinoma HCT116 cells mediated by JNK/p38/ERK1/2 via a p53-independent signaling. Sci Rep. 2019;9(1):11094.

63. Levine GN, Bates ER, Blankenship JC, Bailey SR, Bittl JA, Cercek B, et al. 2015 ACC/AHA/SCAI Focused Update on Primary Percutaneous Coronary Intervention for Patients With ST-Elevation Myocardial Infarction: An Update of the 2011 ACCF/AHA/SCAI Guideline for Percutaneous Coronary Intervention and the 2013 ACCF/AHA Guideline for the Management of ST-Elevation Myocardial Infarction. J Am Coll Cardiol. 2016;67(10):1235-50.

64. Tearney GJ, Regar E, Akasaka T, Adriaenssens T, Barlis P, Bezerra HG, et al. Consensus standards for acquisition, measurement, and reporting of intravascular optical coherence tomography studies: a report from the International Working Group for Intravascular Optical Coherence Tomography Standardization and Validation. J Am Coll Cardiol. 2012;59(12):1058-72.

65. Prati F, Regar E, Mintz GS, Arbustini E, Di Mario C, Jang IK, et al. Expert review document on methodology, terminology, and clinical applications of optical coherence tomography: physical principles, methodology of image acquisition, and clinical application for assessment of coronary arteries and atherosclerosis. Eur Heart J. 2010;31(4):401-15.

Figure legends

Figure 1. Study flow chart. STEMI, ST segment elevation myocardial infarction; HMU, Harbin Medical University; ECG, electrocardiogram; OCT, optical coherence tomography.

Figure 2. IRGM is associated with atherosclerotic plaque rupture in patients with STEMI, and highly expressed in patients with atherosclerotic plaque. (A) Representative OCT images in normal coronary vessels, NO-RUP plaques and RUP plaques; arrows show TCFA, with FCT < 65 μm, as well as lipid arc >90°; asterisks represent ruptured cavities at the culprit site. (B) Serum IRGM levels among healthy volunteers, NO-RUP patients and RUP patients as detected by ELISA. *p<0.05; ##p<0.01; &p<0.05. (C) Adjusted ORs and 95% CIs for plaque rupture associated with serum IRGM in patients with STEMI by 4 models: Model 1, a model adjusted for age; Model 2, in which Model 1 was further adjusted for hypertension, diabetes mellitus and current smoking; Model 3, in which Model 2 was additionally adjusted for lipid factors (LDL-C and TC) and Model 4, in which Model 3 was further adjusted for peak TnI and hs-CRP. (D) Representative images of the detection of the expression of IRGM and CD68 in atherosclerotic plaques and normal vessels of the human lower limbs by immunohistochemistry. H&E staining is also shown. Scale bars=100 μm. (E, F) Quantification of the percentage of $IRGM^+$ and $CD68^+$ areas in intimal plaques between atherosclerotic plaques and normal vessels of the human lower limbs, respectively. *p<0.05; ns=no significance.

Figure 3. Irgm1 can affect atherosclerotic lesion phenotype in vivo. (A) Genotype analyses for IRGM were determined by PCR; Lane 1, 2, 4, 6, 7 and 9 represent $ApoE^{-/-}Irgm1^{+/+}$ mice, Lane 3, 5, 8 and 10 represent $ApoE^{-/-}Irgm1^{+/-}$ mice. (B) Study design for the establishment of advancing atherosclerotic plaques in mice. After being given a

high-fat diet for 16 weeks, mice were sacrificed, and frozen or paraffin slices of tissues prepared for staining. HFD = high-fat diet; wks=weeks. (C, D) Representative images and quantitative analyses of Oil Red O staining in 3 parts of the aorta, namely aortic arch (AA) (n=4), thoracic aorta (TA) (n=4), and abdominal aorta (Ad.A) (n=4). (E) Representative images for H&E staining to assess the FCT, necrotic lipid core as well as plaque areas in the aortic sinus (n=10). Necrotic lipid cores are denoted by *; black dashed lines indicate the contour of the plaques; scale bars=200 μm. (F, G) Quantitative analyses of plaque areas and FCT were measured by ImageJ (n=10). (J) Percentage of necrotic core areas in the plaques (n=10). (H) Neutral lipid was detected in the aortic sinus by ORO staining (n=10); scale bars=200 μm. (I) Representative images for the detection of collagen in the aortic sinus as revealed by Masson staining (n=10); scale bars=200 μm. (K, L) Quantitative analyses of the percentage of neutral lipid and collagen content in the plaques determined by ImageJ, respectively. (M) Representative images of cholesterol crystals observed by confocal microscopy (n=8~9); scale bars=50 and 100 μm. (N) Quantitative analyses of the proportion of cholesterol crystals in the plaque determined by ImageJ. $A^{-}I^{+}$= ApoE$^{-/-}$Irgm1$^{+/+}$ mice; $A^{-}I^{-}$= ApoE$^{-/-}$Irgm1$^{+/-}$ mice; *p<0.05, **p<0.01, ***p<0.001; ns=no significance. Results are presented as the mean ± SD. Statistical analysis: unpaired Student's *t-test*.

Figure 4. Irgm1 induces apoptosis in macrophages. (A) TUNEL^{+} cell areas in aortic sinus plaques from ApoE$^{-/-}$Irgm1$^{+/+}$ (n=3) and ApoE$^{-/-}$Irgm1$^{+/-}$ mice (n=3) detected by immunofluorescence. Areas circled by dashed lines represent for the contour of plaques; scale bars=200 μm. (B) Quantification of the percentage of TUNEL^{+} areas within the plaques measured by ImageJ. (C) Representative images for the detection of cleaved-caspase3 and cleaved-caspase9 in the plaques by immunohistochemistry (n=3); NC=negative control; scale bars=100 μm. (D, E) Quantitative analyses of the percentage of cleaved-caspase3 and cleaved-caspase9 areas in the plaques calculated by ImageJ. (F–G) The Raw264.7 macrophage cells line was first transfected with si-Irgm1, and then stimulated with ox-LDL (50 ng/ml) for 48 h. Proteins were extracted from the cells, and the activity of cleaved-caspase3 (F) and cleaved-caspase9 (G) was quantified. (H) Western blotting was used to detect the expression of cleaved-caspase3 and cleaved-caspase9 in cellular proteins under the same treatment conditions as (F, G), respectively. Duplicate samples were run in the same gels, with the membrane cut in half. GAPDH was used as a loading control. Quantitative data represent the fold change after normalizing cleaved-caspase3 and cleaved-caspase9 band intensity to GAPDH. (I) Quantitative analyses of the expression of cleaved-caspase3 and cleaved-caspase9 detected by western blotting in (H). (J, M) Peritoneal macrophages from ApoE$^{-/-}$Irgm1$^{+/+}$ (n=4) and ApoE$^{-/-}$Irgm1$^{+/-}$ mice (n=4) were recruited after 16 weeks of a high-fat diet, and then FITC-Annexin V and PE-PI were co-stained and quantified by flow cytometry. (K) Representative images for co-location of cleaved-caspase3 (red) and

CD11b (green) by immunofluorescence staining after 16 weeks of a high-fat diet in ApoE$^{-/-}$Irgm1$^{+/+}$ (n=3) and ApoE$^{-/-}$Irgm1$^{+/-}$ mice (n=3). (L) Co-location of cleaved-caspase9 (red) and CD11b (green) by immunofluorescence staining after 16 weeks of a high-fat diet in ApoE$^{-/-}$Irgm1$^{+/+}$ (n=3) and ApoE$^{-/-}$Irgm1$^{+/-}$ mice (n=3); nucleus were stained by DAPI (blue); scale bars=200 μm. (N, O) Quantitative data of the co-location percentage of CD11b^{+} with cleaved-caspase3 (N) and cleaved-caspase9 (O) as detected by immunofluorescence in (K, L), respectively. A^{-}I^{+}= ApoE$^{-/-}$Irgm1$^{+/+}$ mice; A^{-}I^{-}= ApoE$^{-/-}$Irgm1$^{+/-}$ mice, *p<0.05, **P<0.01. Results are presented as the mean ± SD. Statistical analysis: unpaired Student's *t-test*。

Figure 5. ROS contributes to Irgm1-induced apoptosis in macrophages. (A) The Raw264.7 macrophage cell line was first transfected with si-Irgm1 and si-control, then stimulated with ox-LDL (50 μg/ml) for 48 h. Representative images of the reactive oxygen species labeled with DHE (5 μM) fluorescent probe were observed by confocal microscopy (n=3 per group); scale bars=50 μm. (B) Quantitative data in the graph represent relative mean fluorescence intensity (MFI) (n=3 per group). (D) The Raw264.7 cell line was first transfected with si-Irgm1 and si-control, followed by stimulation with ox-LDL (50 μg/ml) for 48 h. Flow cytometry was used to detect ROS labeled with DHE fluorescent probes (n=6 per group). (C) Quantitative data represent the percentage of DHE^+ macrophages (n=6 per group). (E) After stimulation with ox-LDL (50 μg/ml) for 48 h, western blotting was used to detect the expression of cleaved-caspase3 and cleaved-caspase9 among the three groups, namely si-control, si-Irgm1 and si-Irgm1 with NAC (an ROS scavenger). Duplicate samples were run in the same gels, with the membrane cut in half. GAPDH was used as a loading control. (F) Quantitative data represent the fold change after normalizing cleaved-caspase3 and cleaved-caspase9 band intensity to GAPDH. (G, H) The protein activity of cleaved-caspase3 and cleaved-caspase9 was detected by ultraviolet spectrophotometry, under the same conditions as shown in (E) (n=3 per group). (I) Representative images for $TUNEL^+$ macrophages (green) by immunofluorescence. nuclei were stained by DAPI (blue). DIC channel shown the contour of cells; scale bars= 50 μm. (J) Quantitative data in the graph represent relative mean fluorescence intensity (MFI) (n=3 per group). si-

control vs. si-Irgm1, *$p<0.05$, **$p<0.01$; si-Irgm1 vs. si-Irgm1+NAC, #$p<0.05$, ##$p<0.01$. Results are presented as the mean ± SD. Statistical analysis: unpaired Student's *t-test*。

Figure 6. Irgm1 induces apoptosis in macrophages by activating the MAPK signaling pathways. (A) The expression of p-JNK, p-38, p-ERK and apoptosis-related Bax, Bcl2, cleaved-caspase3 and cleaved-caspase9 in si-control, si-Irgm1 and si-Irgm1 cells treated with NAC as detected by western blotting, after stimulating with ox-LDL (50 μg/ml) for 48 h. GAPDH was used as a loading control. (B, C) Quantitative data representing the fold change after normalizing band intensity of p-JNK, p-p38, p-ERK, Bax, Bcl2, cleaved-caspase3 and cleaved-caspase9 to GAPDH. (D) The expression of Bax, Bcl2, cleaved-caspase3 and cleaved-caspase9 as detected by western blotting in si-control (Lane 1–5) and si-Irgm1 (Lane 6–10) groups, after treatment with SP600125 (an inhibitor of JNK signaling), SB203580 (an inhibitor of p38 signaling) and U0126 (an inhibitor of ERK 1/2 signaling). Lane 3 and 8 represent treatment with SP600125 (10 μM) for 3 h. Lane 4 and 9 represent treatment with SB203580 (10 μM) for 3 h. Lane 5 and 10 represent treatment with U0126 (10 μM) for 3 h. GAPDH was used as a loading control. (E–H) Quantitative data representing the fold change after normalizing band intensity of Bax, Bcl2, cleaved-caspase3 and cleaved-caspase9 to GAPDH. si-control vs. si-Irgm1 in (B, C): *$p<0.05$, **$p<0.01$, ***$p<0.001$,****$p<0.0001$; si-Irgm1 vs. si-Irgm1+NAC, #$p<0.05$, ##$p<0.01$; si-control vs. si-Irgm1 in (D–H): Lane 1 vs. Lane 2, Lane 6 vs. Lane 7, *$p<0.05$, **$p<0.01$, ***$p<0.001$; Lane 3, 4, 5 vs. Lane 2; Lane 8, 9, 10 vs. Lane 7, &$p<0.05$, &&$p<0.01$. Results are presented as the mean ± SD. Statistical analysis: unpaired Student's *t-test*.

Figure 7. Irgm1 aggravates plaque progression in bone marrow chimera recipient mice and contributes to macrophage apoptosis. (A) Schematic diagram for the establishment of the bone marrow chimera recipient mouse model. C57BL/6 mice were fed sterile pH 3.0 water supplemented with polymyxin and fradiomycin,, from one week before radiation till the end of the experiment. Bone marrow monocytes (5×10^6) from ApoE$^{-/-}$Irgm1$^{+/+}$ and ApoE$^{-/-}$Irgm1$^{+/-}$ donor mice were extracted and injected back into recipient mice (irradiated with 9 Gys radiation). The model of advanced atherosclerosis was established after the animals were given a high-fat diet for 16 weeks. (B) Representative images of cholesterol crystals observed by confocal microscopy from ApoE$^{-/-}$Irgm1$^{+/+}$ (n=3) and ApoE$^{-/-}$Irgm1$^{+/-}$ (n=3) bone marrow chimera recipient mice; scale bars=100 μm. (C) Quantitative analyses of the proportion of cholesterol crystals in the plaque as determined by ImageJ. (D) Representative images for H&E staining of plaques in the aortic sinus from ApoE$^{-/-}$Irgm1$^{+/+}$ (n=5) and ApoE$^{-/-}$Irgm1$^{+/-}$ (n=3) bone marrow chimera recipient mice. A necrotic lipid core is indicated by *; dashed lines indicate the contour of the plaques; scale bars=200 μm. (E, H) Quantitative analyses of FCT, and percentage of necrotic core areas in the plaques as measured by ImageJ. (F) Representative images of neutral lipid detected in the aortic sinus by ORO staining from ApoE$^{-/-}$Irgm1$^{+/+}$ (n=5) and ApoE$^{-/-}$Irgm1$^{+/-}$ (n=3) bone marrow chimera recipient mice; scale bars=200 μm. (G) Representative images for the detection of collagen in the aortic sinus by Masson staining from ApoE$^{-/-}$Irgm1$^{+/+}$ (n=5) and ApoE$^{-/-}$Irgm1$^{+/-}$ (n=3) bone marrow chimera recipient mice; scale bars=200 μm. (I, J)

Quantitative analyses of the percentage of neutral lipid and collagen content in the plaques as determined by ImageJ, respectively. (K) Representative images for detection of cleaved-caspase3 in aortic sinus plaques by immunohistochemistry. NC=negative control; scale bars=100 μm. (L) Quantitative data for the percentage of cleaved-caspase3^{+} area in the plaques as measured by ImageJ. (M) After being fed a high-fat diet for 16 weeks, ApoE$^{-/-}$Irgm1$^{+/+}$ (n=5) and ApoE$^{-/-}$Irgm1$^{+/-}$ (n=3) bone marrow chimera recipient mice were sacrificed and protein from the aortic arch extracted. The expression of cleaved-caspase3 and cleaved-caspase9 was detected by western blotting. GAPDH was used as a loading control. (N) Quantitative data represent the fold change after normalizing band intensity of cleaved-caspase3 and cleaved-caspase9 to GAPDH.ApoE$^{-/-}$Irgm1$^{+/+}$ vs. ApoE$^{-/-}$Irgm1$^{+/-}$, *p<0.05, **p<0.01. Results are presented as the mean ± SD. Statistical analysis: unpaired Student's *t-test*.

Figure 8. Summary of the role of IRGM/Irgm1 in atherosclerotic plaque progression by promoting macrophage apoptosis.

During the progression of atherosclerotic plaque, ox-LDL is continuously engulfed by the increasing number of macrophages. The expression of IRGM/Irgm1 in macrophages increases rapidly, which promotes the production of ROS, activates the MAPK signaling pathway, and finally induces macrophage apoptosis. The stability of the plaque then changes with the increase in the content of necrotic core, lipid, and cholesterol crystals, fibrous cap thinning, and collagen fibers decrease, transforming the plaque from stable to vulnerable. Such a vicious circle leads to further plaque progression and eventually plaque rupture.

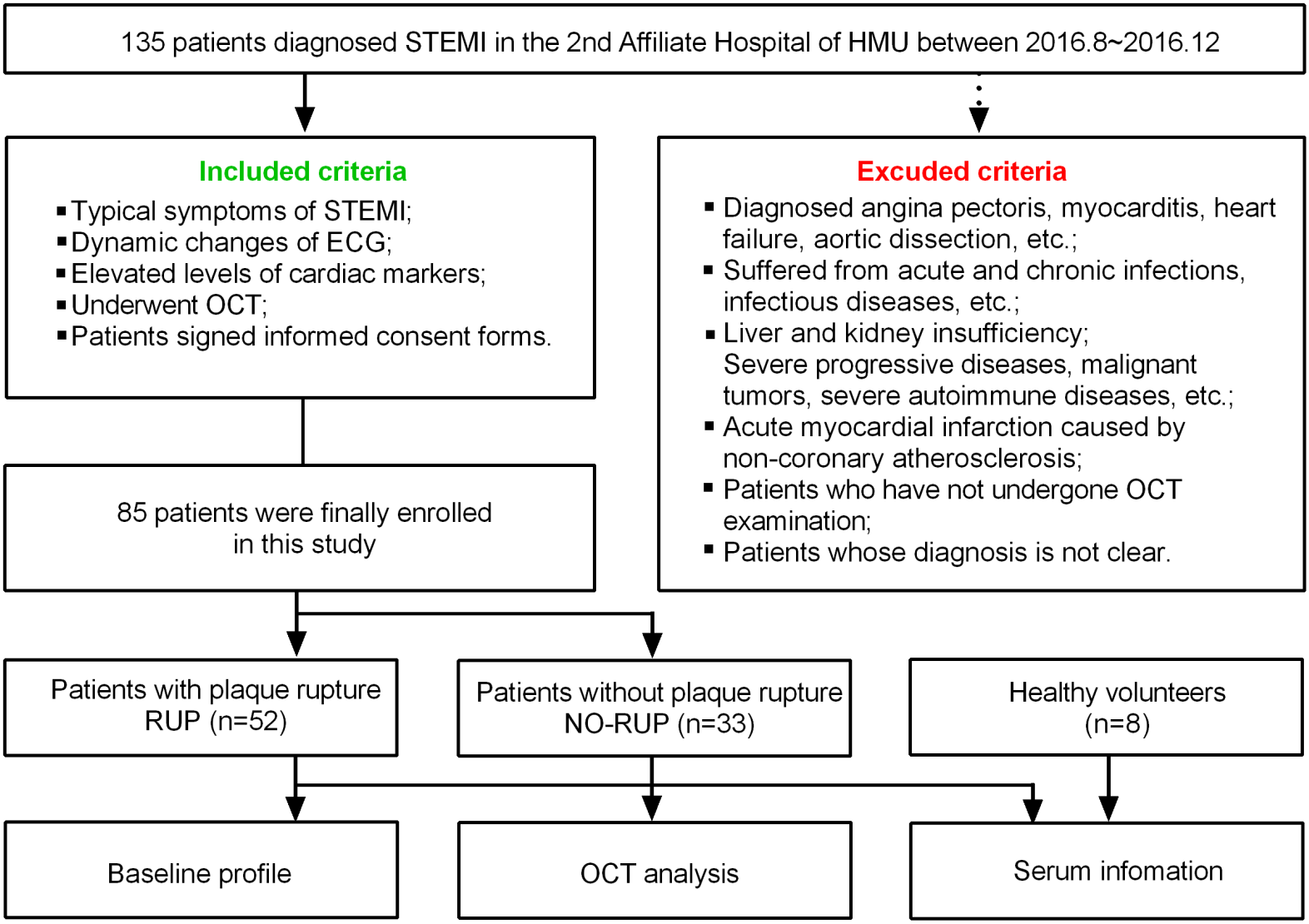
135 patients diagnosed STEMI in the 2nd Affiliate Hospital of HMU between 2016.8~2016.12
Included criteria
Typical symptoms of STEMI;
Dynamic changes of ECG;
Elevated levels of cardiac markers;
Underwent OCT;
Patients signed informed consent forms.
Excuded criteria
Diagnosed angina pectoris, myocarditis, heart failure, aortic dissection, etc.;
Suffered from acute and chronic infections, infectious diseases, etc.;
Liver and kidney insufficiency;
Severe progressive diseases, malignant tumors, severe autoimmune diseases, etc.;
Acute myocardial infarction caused by non-coronary atherosclerosis;
Patients who have not undergone OCT examination;
Patients whose diagnosis is not clear.
85 patients were finally enrolled in this study
Patients with plaque rupture RUP (n=52)
Patients without plaque rupture NO-RUP (n=33)
Healthy volunteers (n=8)
Baseline profile
OCT analysis
Serum infomation

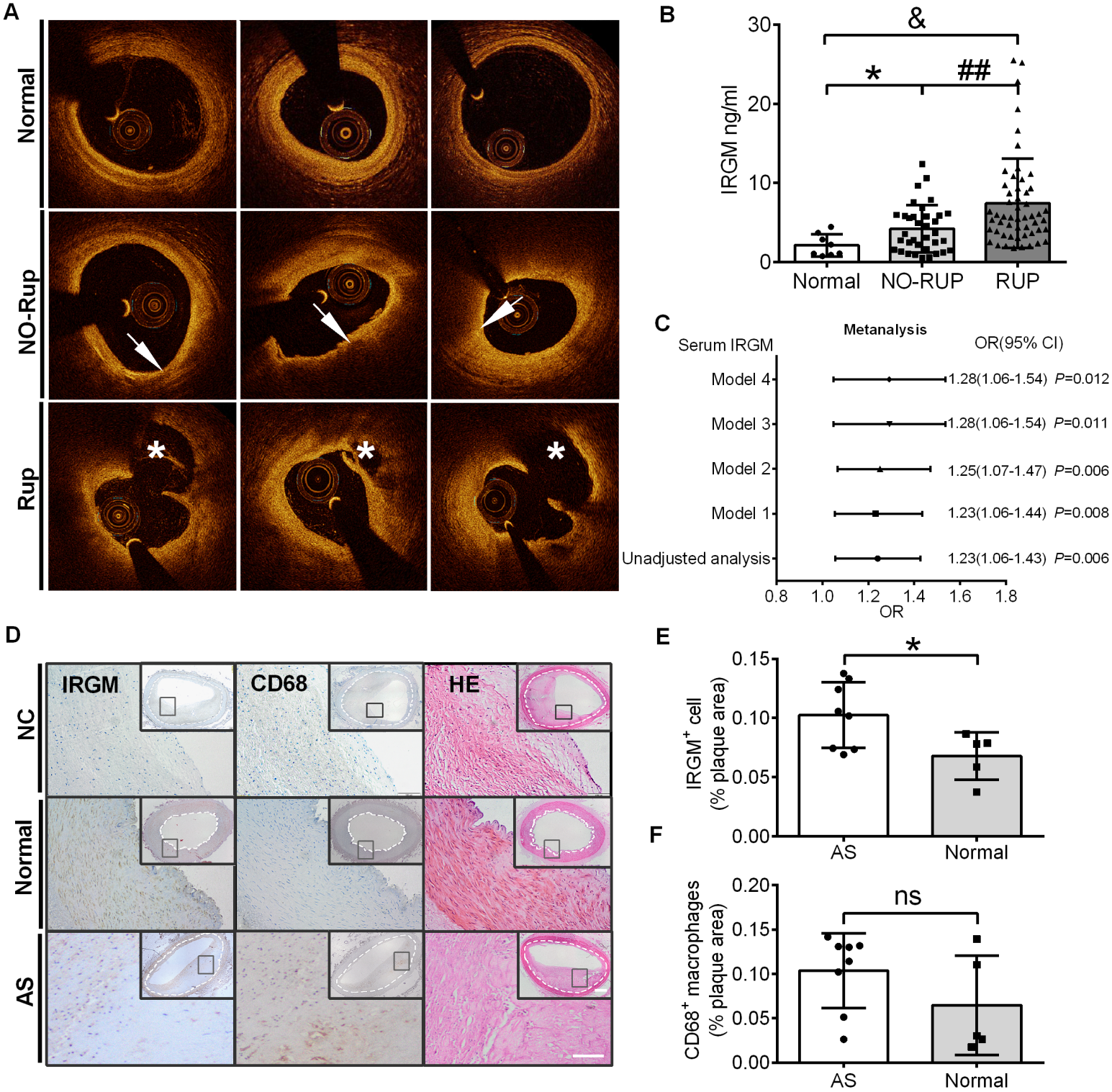
A
Normal
NO-Rup
Rup
B
IRGM ng/ml
30
20
10
0
&
*
##
Normal
NO-RUP
RUP
C
Metanalysis
Serum IRGM
OR(95% CI)
Model 4
1.28(1.06-1.54) P=0.012
Model 3
1.28(1.06-1.54) P=0.011
Model 2
1.25(1.07-1.47) P=0.006
Model 1
1.23(1.06-1.44) P=0.008
Unadjusted analysis
1.23(1.06-1.43) P=0.006
0.8
1.0
1.2
1.4
1.6
1.8
OR
D
IRGM
CD68
HE
NC
Normal
AS
E
IRGM+ cell (% plaque area)
0.15
0.10
0.05
0.00
*
AS
Normal
F
CD68+ macrophages (% plaque area)
0.20
0.15
0.10
0.05
0.00
ns
AS
Normal

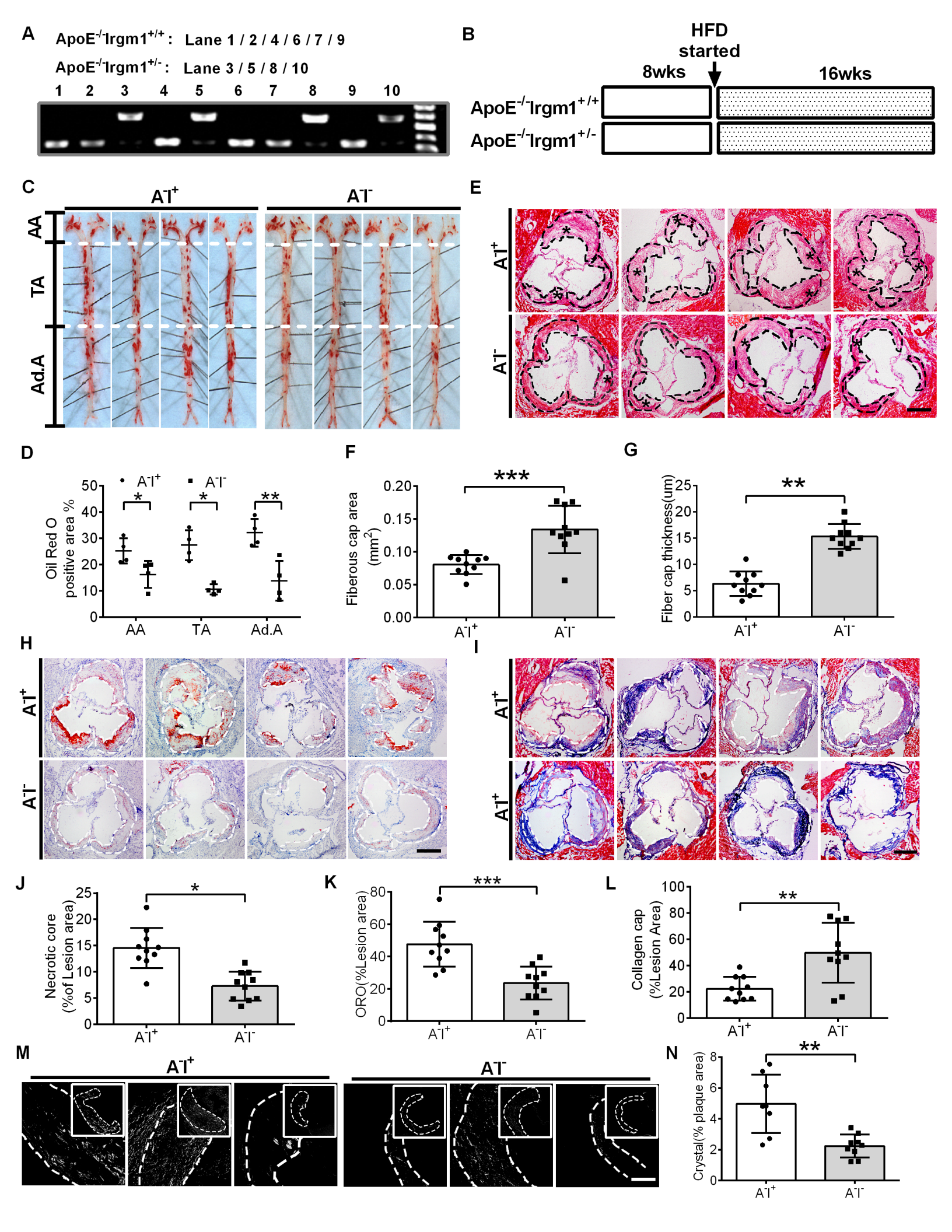
A
ApoE-/-Irgm1+/+ : Lane 1 / 2 / 4 / 6 / 7 / 9
ApoE-/-Irgm1+/- : Lane 3 / 5 / 8 / 10
1 2 3 4 5 6 7 8 9 10
B
HFD started
8wks
16wks
ApoE-/-Irgm1+/+
ApoE-/-Irgm1+/-
C
A-I+
A-I-
AA
TA
Ad.A
E
A-I+
A-I-
D
A-I+
A-I-
Oil Red O positive area %
AA
TA
Ad.A
F
Fiberous cap area (mm2)
A-I+
A-I-
G
Fiber cap thickness(um)
A-I+
A-I-
H
A-I+
A-I-
I
A-I+
A-I+
J
Necrotic core (%of Lesion area)
A-I+
A-I-
K
ORO(%Lesion area)
A-I+
A-I-
L
Collagen cap (%Lesion Area)
A-I+
A-I-
M
A-I+
A-I-
N
Crystal(% plaque area)
A-I+
A-I-

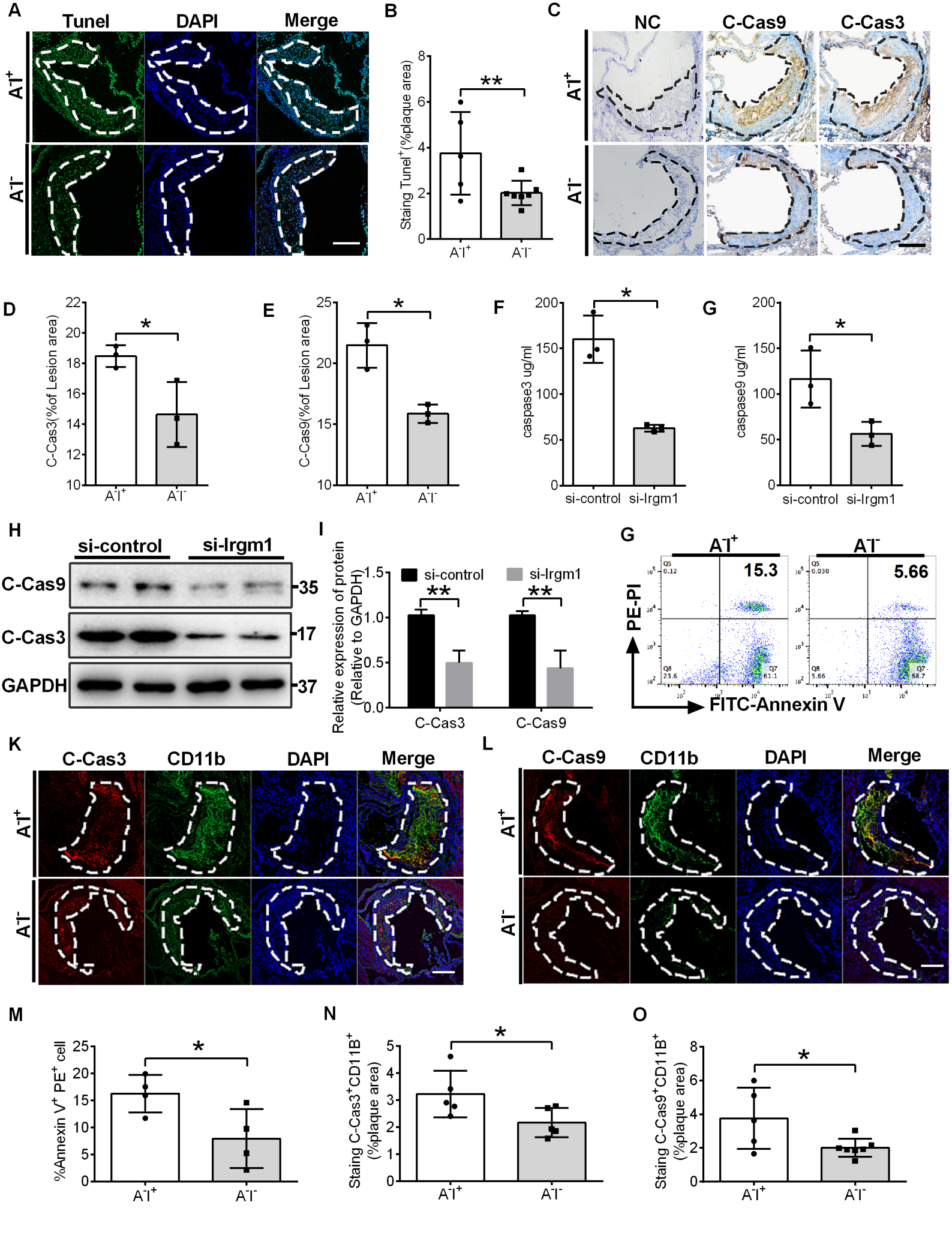
A
Tunel
DAPI
Merge
A-I+
A-I-
B
Staing Tunel+(%plaque area)
**
C
NC
C-Cas9
C-Cas3
D
C-Cas3(%of Lesion area)
*
E
C-Cas9(%of Lesion area)
F
caspase3 ug/ml
si-control
si-lrgm1
G
caspase9 ug/ml
H
si-control
si-lrgm1
C-Cas9
C-Cas3
GAPDH
35
17
37
I
Relative expression of protein (Relative to GAPDH)
si-control
si-lrgm1
C-Cas3
C-Cas9
G
15.3
5.66
PE-PI
FITC-Annexin V
K
C-Cas3
CD11b
DAPI
Merge
L
C-Cas9
M
%Annexin V+ PE+ cell
N
Staing C-Cas3+CD11B+ (%plaque area)
O
Staing C-Cas9+CD11B+ (%plaque area)

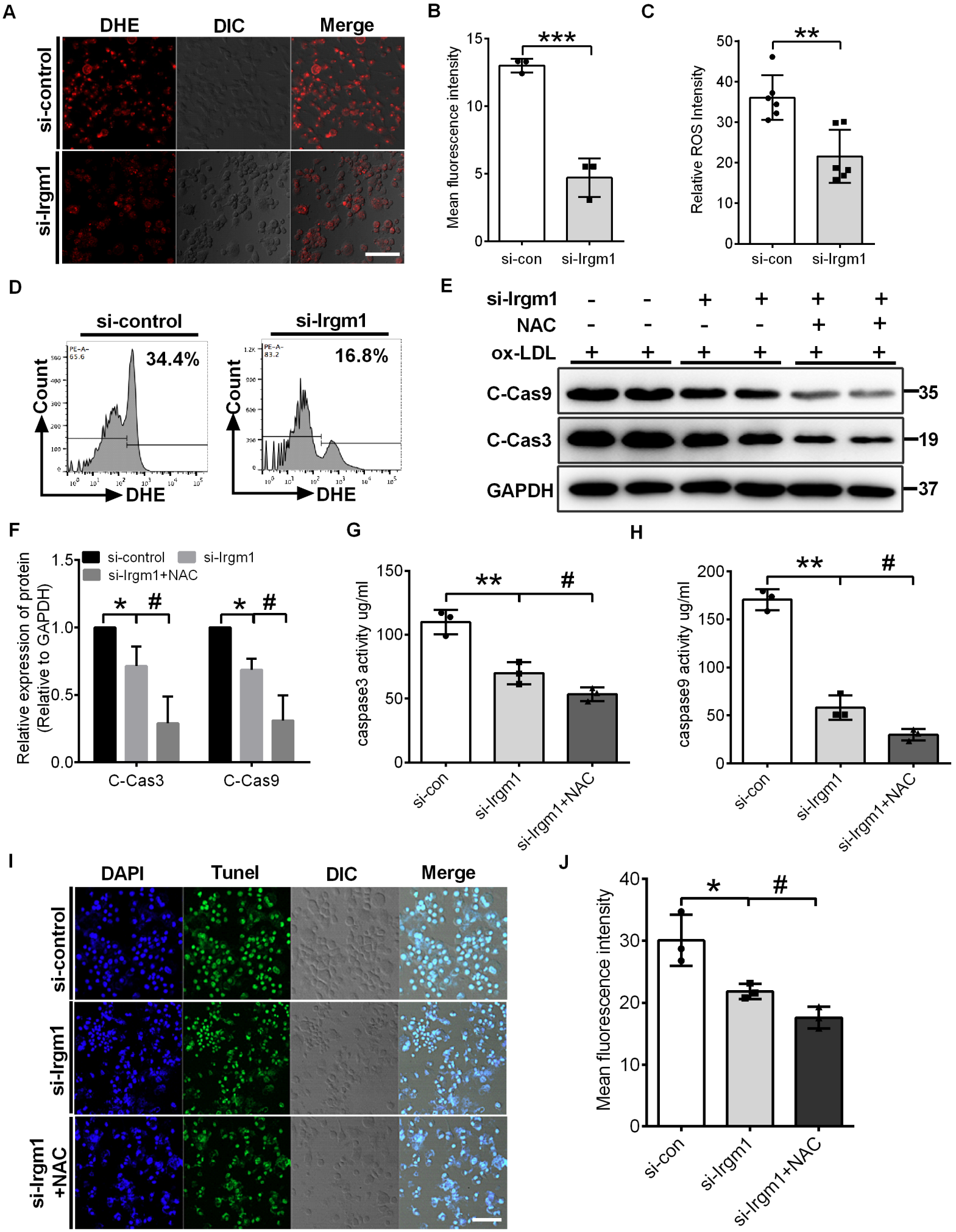
A
DHE
DIC
Merge
si-control
si-lrgm1
B
Mean fluorescence intensity
***
si-con
si-lrgm1
C
Relative ROS Intensity
**
si-con
si-lrgm1
D
si-control
si-lrgm1
34.4%
16.8%
Count
DHE
E
si-lrgm1
NAC
ox-LDL
C-Cas9
C-Cas3
GAPDH
35
19
37
F
si-control
si-lrgm1
si-lrgm1+NAC
Relative expression of protein (Relative to GAPDH)
C-Cas3
C-Cas9
G
caspase3 activity ug/ml
si-con
si-lrgm1
si-lrgm1+NAC
H
caspase9 activity ug/ml
si-con
si-lrgm1
si-lrgm1+NAC
I
DAPI
Tunel
DIC
Merge
si-control
si-lrgm1
si-lrgm1 +NAC
J
Mean fluorescence intensity
si-con
si-lrgm1
si-lrgm1+NAC

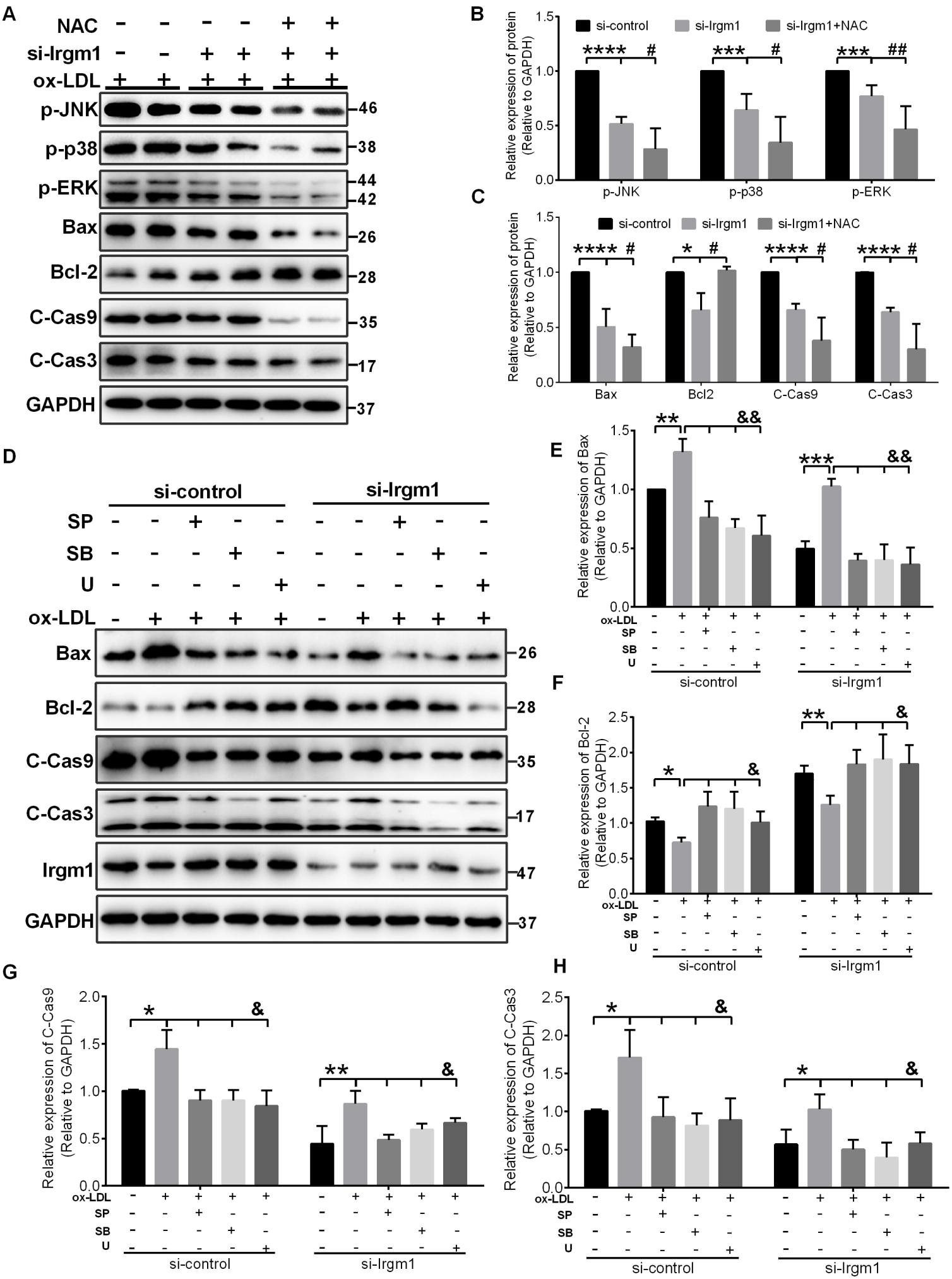
A
NAC
si-Irgm1
ox-LDL
p-JNK
p-p38
p-ERK
Bax
Bcl-2
C-Cas9
C-Cas3
GAPDH
46
38
44
42
26
28
35
17
37
B
si-control
si-Irgm1
si-Irgm1+NAC
Relative expression of protein (Relative to GAPDH)
p-JNK
p-p38
p-ERK
C
Bax
Bcl2
C-Cas9
C-Cas3
D
si-control
si-Irgm1
SP
SB
U
ox-LDL
Bax
Bcl-2
C-Cas9
C-Cas3
Irgm1
GAPDH
26
28
35
17
47
37
E
Relative expression of Bax (Relative to GAPDH)
F
Relative expression of Bcl-2 (Relative to GAPDH)
G
Relative expression of C-Cas9 (Relative to GAPDH)
H
Relative expression of C-Cas3 (Relative to GAPDH)

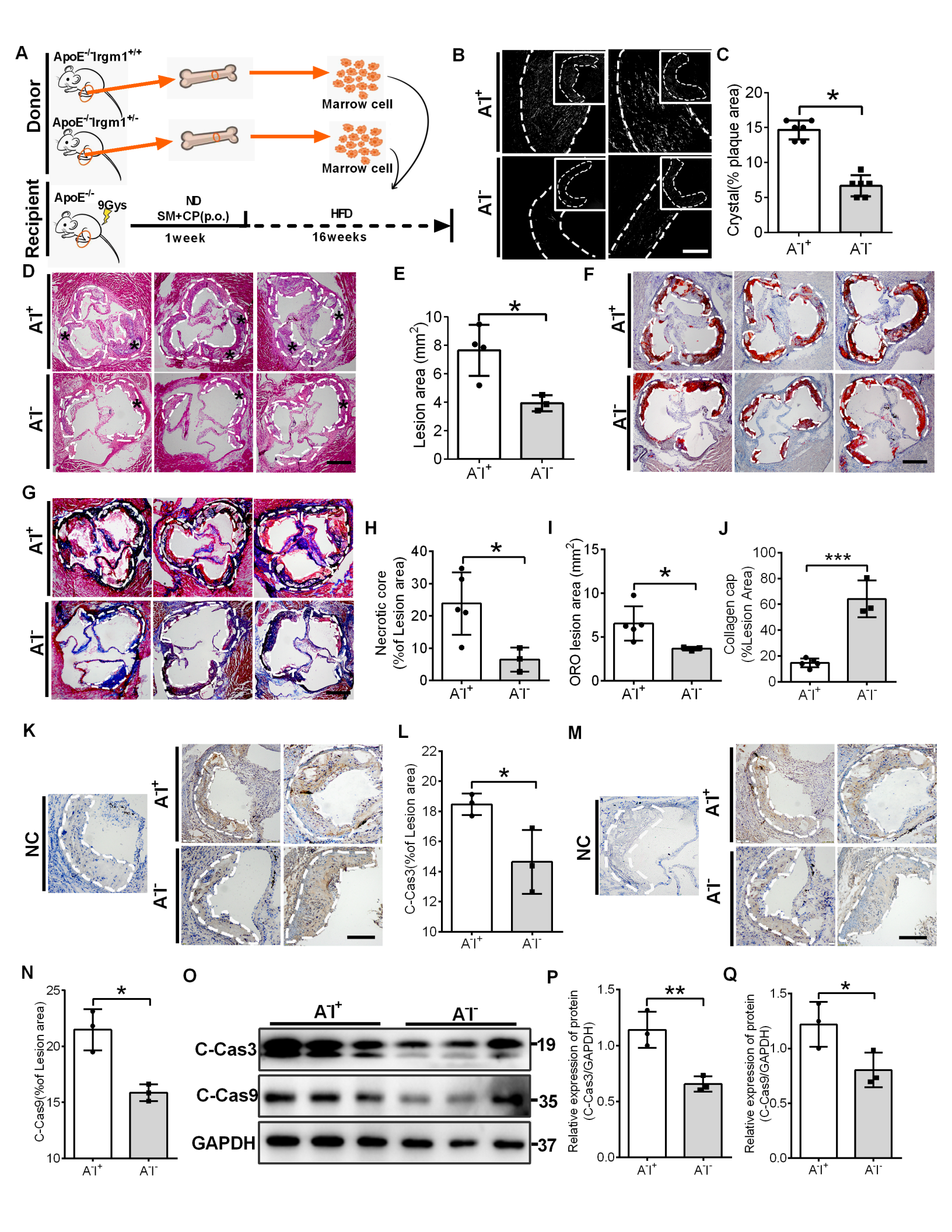
A
Donor
ApoE-/-Irgm1+/+
ApoE-/-Irgm1+/-
Marrow cell
Marrow cell
Recipient
ApoE-/-
9Gys
ND
SM+CP(p.o.)
1week
HFD
16weeks
B
A-I+
A-I-
C
Crystal(% plaque area)
A-I+
A-I-
D
E
Lesion area (mm2)
F
G
H
Necrotic core (%of Lesion area)
I
ORO lesion area (mm2)
J
Collagen cap (%Lesion Area)
K
NC
L
C-Cas3(%of Lesion area)
M
N
C-Cas9(%of Lesion area)
O
C-Cas3
C-Cas9
GAPDH
19
35
37
P
Relative expression of protein (C-Cas3/GAPDH)
Q
Relative expression of protein (C-Cas9/GAPDH)

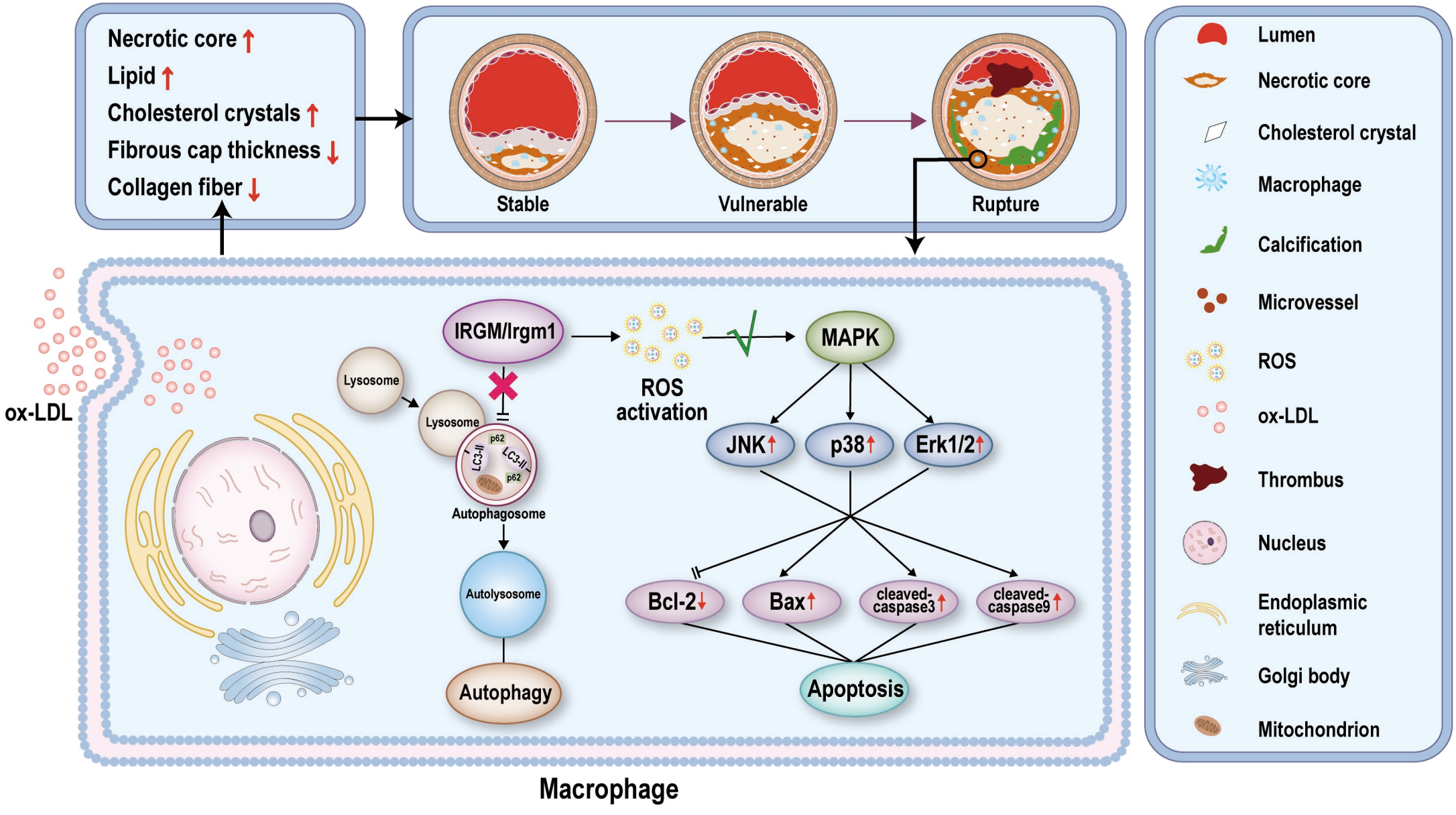
Necrotic core ↑
Lipid ↑
Cholesterol crystals ↑
Fibrous cap thickness ↓
Collagen fiber ↓
Stable
Vulnerable
Rupture
ox-LDL
IRGM/Irgm1
Lysosome
Lysosome
p62
LC3-I
LC3-II
p62
Autophagosome
Autolysosome
Autophagy
ROS
activation
MAPK
JNK↑
p38↑
Erk1/2↑
Bcl-2↓
Bax↑
cleaved-caspase3↑
cleaved-caspase9↑
Apoptosis
Macrophage
Lumen
Necrotic core
Cholesterol crystal
Macrophage
Calcification
Microvessel
ROS
ox-LDL
Thrombus
Nucleus
Endoplasmic reticulum
Golgi body
Mitochondrion